

Accurate CMB covariance matrices: exact calculation and approximations

E. Camphuis¹, K. Benabed¹, S. Galli¹, E. Hivon¹, and M. Lilley²

¹ Sorbonne Université, UMR7095, Institut d’Astrophysique de Paris, 98 bis Boulevard Arago, F-75014, Paris, France

² SYRTE, Observatoire de Paris, Université PSL, CNRS, Sorbonne Université, LNE, 61 avenue de l’Observatoire 75014 Paris, France

May 2, 2022

ABSTRACT

Accurate covariance matrices are required for a reliable estimation of cosmological parameters from pseudo-power spectrum estimators. In this work, we focus on the analytical calculation of covariance matrices. We consider the case of observations of the Cosmic Microwave Background in temperature and polarization on a small footprint such as in the SPT-3G experiment, which observes 4% of the sky. Power spectra evaluated on small footprints are expected to have large correlations between modes, and these need to be accurately modelled. We present, for the first time, an algorithm that allows an efficient (but computationally expensive) exact calculation of analytic covariance matrices. Using it as our reference, we test the accuracy of existing fast approximations of the covariance matrix. We find that, when the power spectrum is binned in wide bandpowers, current approaches are correct up to the 5% level on the SPT-3G small sky footprint. Furthermore, we propose a new approximation which improves over the previous ones reaching a precision of 1% in the wide bandpowers case and generally more than 4 times more accurate than current approaches. Finally, we derive the covariance matrices for mask-corrected power spectra estimated by the PolSpice code. In particular, we include, in the case of a small sky fraction, the effect of the apodization of the large scale modes. While we considered the specific case of the CMB, our results are applicable to any other cosmological probe which requires the calculation of pseudo-power spectrum covariance matrices.

Key words. cosmic background radiation – cosmology: observations – cosmological parameters – methods: data analysis

1. Introduction

One of the most powerful probes of cosmology is the observation of the Cosmic Microwave Background (CMB) anisotropies. The ESA Planck satellite CMB measurements marked the entry into the era of precision cosmology, with many Λ CDM cosmological parameters measured with uncertainties smaller than 1% (Planck Collaboration et al. 2020). Ongoing and upcoming ground-based and satellite experiments such as the Atacama Cosmology Telescope (ACT) (Aiola et al. 2020), the South Pole Telescope (SPT) (Dutcher et al. 2021), Simons Observatory (SO) (Ade et al. 2019), CMB-Stage 4 (CMB-S4) (Abazajian et al. 2016) and Litebird (Hazumi et al. 2012) will provide yet more information about the nature of our universe.

Since primary CMB anisotropies in intensity and polarization are distributed as a gaussian random field, most of the cosmological information is contained in the angular power spectrum of the CMB anisotropies. As the evolution of the primary anisotropies is linear, the multipoles of the angular power spectrum are uncorrelated when observing the full sky. However, any realistic experiment requires masking parts of the sky, either to avoid regions highly contaminated by foregrounds (such as galactic emission or point sources), or because the scanning strategy is designed to observe specific regions of the sky. The estimation of the power spectrum on the masked sky, the so-called pseudo-power spectrum, is biased and different multipoles become correlated (Hivon et al. 2002). An unbiased estimator of the spectra can then be obtained through the MASTER approach (Hivon et al. 2002), as implemented e.g. in the PolSpice¹ software (Szapudi et al. 2001; Chon et al. 2004). A robust inference

of cosmological parameters requires accurate covariance matrices that describe the variance of the spectra along their diagonal, as well as the correlations between multipoles in the off-diagonal terms. Pseudo- C_ℓ covariance matrices are corrected for the effect of the mask using MASTER to obtain the covariance matrices for the unbiased C_ℓ estimator. Inaccuracies in the covariance matrix estimation can lead to the misestimation of cosmological parameters and of their uncertainties (Dodelson & Schneider 2013; Sellentin & Starck 2019).

Covariance matrices can be calculated through the use of simulations. The number of simulations determines the accuracy of the estimator. As the simulations are expensive to produce, the obtained noisy realization of the covariance has to be regularized (Balkenhol & Reichardt 2021)². Alternatively, it is possible to calculate pseudo- C_ℓ covariance matrices analytically. However, these depend on integrals whose exact numerical implementation is computationally expensive. Thus, approximations have been proposed in previous works to make these calculations efficient, see e.g. Efstathiou (2004); Nicola et al. (2021); Friedrich et al. (2021).

We analyze the problem of computing accurate analytical covariance matrices. We take the specific case of the SPT-3G experiment, which observes the CMB anisotropies in temperature and polarization on a small sky patch, which corresponds to about 4% of the sky. On such a small sky region, the calculated power spectra has large correlations between multipoles. The existing approximations of the covariance matrix can be less accurate

¹<http://www2.iap.fr/users/hivon/software/PolSpice/>

²While this work focuses on covariance estimates obtained through empirical estimators, the conditioning schemes it presents can similarly be applied to estimates from simulations.

rate in these conditions. Considering this particular case is thus a particularly stringent test of the validity of analytical algorithms.

We implement for the first time the exact computationally expensive calculation of the covariance matrices, which we find to be numerically feasible at multipoles smaller than $\ell \lesssim \ell_{\max, \text{ex}} \equiv 1000$ thanks to a new algorithm that gains one order of numerical complexity over the brute-force approach, resulting in a thousand-fold speed improvement. Then, we test the existing approximations, and find that they are accurate at the 5% level in the case of the SPT-3G footprint when the power spectrum is averaged in wide bandpowers. We then propose a new approximation which improves over the existing algorithms to attain an accuracy of 1% in the same case. Finally, we describe how to calculate the covariance matrix of the PolSpice C_ℓ estimator from the pseudo- C_ℓ covariance matrix.

While in this work we focused on the specific case of the SPT-3G CMB experiment, many considerations can be applied more broadly to any probe relying on the calculation of power spectra and covariance matrices.

The paper is organized as follows. In Sect. 2, we introduce the pseudo-power spectrum estimator and its covariance. In Sect. 3 we show how to perform the exact calculation of the covariance matrix. In Sect. 4 we describe the existing approximations for the calculation of the covariance matrix and we test their accuracy against the exact computation. Section 5 presents our new approximation which is more accurate. Sect. 6 describes how to calculate the covariance matrix of the PolSpice estimator. We conclude in Sect. 7, and some detailed calculations are given in the appendices.

2. Covariance of the pseudo-power spectrum

2.1. Pseudo-power spectrum

CMB anisotropies in intensity and polarization can be described as maps of Stokes parameters $T(\hat{n}), Q(\hat{n}), U(\hat{n})$ for a direction \hat{n} of the sky. They are gaussian random fields, fully characterized by their angular power spectra ($C_\ell^{\text{TT}}, C_\ell^{\text{EE}}, C_\ell^{\text{BB}}, C_\ell^{\text{TE}}$), which are the variances of the harmonic coefficients $a_{\ell m}^{\text{T}}, a_{\ell m}^{\text{E}}, a_{\ell m}^{\text{B}}$ obtained by spherical harmonic decomposition of the maps. Cosmological models allow the computation of the expectation of the different power spectra in an ideal full-sky case. However, data only ever covers a part of the sky. We describe the partial coverage with the weight map $W(\hat{n})$. The power spectrum of masked maps, labelled $\tilde{C}_\ell^{\text{XY}}$, is usually called *pseudo-power spectrum*. Its expression for temperature is given in Eq. (A.6). It can be computed from the masked harmonic coefficients $\tilde{a}_{\ell m}^{\text{X}}$ which are directly related to the unmasked ones, $a_{\ell m'}^{\text{X}}$, by the application of the mode coupling kernels ${}_s I_{\ell m \ell' m'}[W]$. In the case of temperature, we write

$$\tilde{a}_{\ell m}^{\text{T}} = \sum_{\ell' m'} a_{\ell' m'}^{\text{T}} {}_0 I_{\ell m \ell' m'}[W], \quad (1)$$

where we have defined the mode coupling kernels³

$${}_s I_{\ell m \ell' m'}[W] \equiv \int d\hat{u}_s Y_{\ell m}(\hat{u}) W(\hat{u}) {}_s Y_{\ell' m'}^*(\hat{u}). \quad (2)$$

These coupling kernels are an important component of the following discussions⁴. In the full-sky case, the closing relations of

spin-weighted spherical harmonics will ensure that ${}_s I_{\ell m \ell' m'}[1] = \delta_{\ell \ell'} \delta_{mm'}$. We recall in App. A some summation properties of products of coupling matrices that appear in the computation of pseudo-power spectra and their covariance. In particular, they are related to the symmetric coupling kernel acting on a power spectrum \mathcal{A} , labelled $\Xi[\mathcal{A}]$, with

$$\Xi_{\ell \ell'}^{ss'}[\mathcal{A}] \equiv \sum_L \frac{2L+1}{4\pi} \mathcal{A}_L \begin{pmatrix} \ell & \ell' & L \\ s & -s & 0 \end{pmatrix} \begin{pmatrix} \ell & \ell' & L \\ s' & -s' & 0 \end{pmatrix}. \quad (3)$$

This operator, introduced in Efstathiou (2004), can also be seen as acting on a map A with power spectrum \mathcal{A}_ℓ . In the following, we will use the notation $\Xi[A] \equiv \Xi[\mathcal{A}]$. We recall that the average of the pseudo-spectrum is related to the underlying power spectrum by the application of the asymmetric coupling kernel computed for the mask W , also known as the MASTER mode-coupling matrix M . In the case of temperature, we have

$$\langle \tilde{C}_\ell^{\text{TT}} \rangle = \sum_{\ell'} {}_0 M_{\ell \ell'}[W] C_{\ell'}^{\text{TT}} \quad (4)$$

$${}_0 M_{\ell \ell'}[W] \equiv (2\ell' + 1) \Xi_{\ell \ell'}^{00}[W]. \quad (5)$$

In this work, without loss of generality, we will develop the computations for the intensity case (*i.e.* $s = s' = 0$), the polarization case being similar. We will also assume that a single mask is used for both temperature and polarization. When required, we will highlight the differences between the temperature and polarization cases and give insight on the importance of the single mask assumption.

2.2. Covariance

Estimating the covariance of the measured power-spectrum is crucial to assess the agreement between data and model predictions and to constrain cosmological parameters from CMB maps. As discussed in Hivon et al. (2002) and demonstrated in App. A, masking breaks statistical isotropy and induces correlations between the modes of the pseudo-spectrum. The details of the derivation of the analytical expression of the pseudo-spectrum covariance can be found in App. B. We give here the expression in terms of the coupling matrices ${}_0 I$ and the true underlying intensity power spectrum C_ℓ , for the temperature case,

$$\begin{aligned} \tilde{\Xi}_{\ell \ell'} &\equiv \text{cov}(\tilde{C}_\ell, \tilde{C}_{\ell'}), \\ &= \frac{2}{(2\ell + 1)(2\ell' + 1)} \sum_{mm'} \sum_{\ell_1 m_1} \sum_{\ell_2 m_2} C_{\ell_1} C_{\ell_2} \\ &\quad {}_0 I_{\ell m \ell_1 m_1}[W] {}_0 I_{\ell' m' \ell_1 m_1}^*[W] {}_0 I_{\ell m \ell_2 m_2}[W] {}_0 I_{\ell' m' \ell_2 m_2}^*[W]. \end{aligned} \quad (6)$$

As shown in Eq. (1), the mode-coupling coefficients ${}_0 I$ kernels relate the underlying harmonic coefficients to the harmonic coefficients measured on the sky through the mask. In the analytic expression of the covariance, they represent the coupling between modes due to partial sky coverage. An expression similar to Eq. (6) can be written for polarization, using spin-2 spherical harmonics, *i.e.* $s, s' = \pm 2$. Those expressions will mix the EE and BB power spectra.

The expression in Eq. (6) involves several convolutions and its evaluation is computationally expensive. The full computation scales as $\mathcal{O}(\ell_{\max}^6)$, ℓ_{\max} being the largest multipole, making the exact computation of this covariance a daunting task given the currently available computation power. We have developed

³The complex conjugate is denoted with a star.

⁴This coupling matrix is often denoted K in the literature such as in Hivon et al. (2002). In this work, we modified the notation for it to be consistent with the notation of Sect. 6.

an algorithm that allows the computation of the covariance matrix at low multipoles with a gain of an order of magnitude in computational time. We discuss this result in Sect. 3.

With such an approach previously unavailable, existing work has relied on approximations of Eq. (6). In Sect. 4 we will present different approximations that have been proposed in previous works and we will then validate them against our full computation. This validation will be performed for a small survey footprint, where spectral modes are highly correlated. These correlations can challenge the assumptions made in the different approximations. Throughout this work, we use a test-case inspired by SPT-3G. The footprint of the first year survey presented in Dutcher et al. (2021) covers roughly 4% of the sky and is displayed in Fig. 1 along with the mask power spectrum \mathcal{W}_ℓ . We apodize the mask with a Gaussian window function of 30 arcmin full width half maximum, using an algorithm similar to the one used in *Planck* Aghanim et al. (2020). We also show in Fig. 1 the power spectrum of one of the masks used in the *Planck* cosmological analysis, which covers a much larger patch of the sky, around 70% before apodization. The precision of the standard approximation of the covariance was validated in the latter case, but it needs to be assessed for a smaller survey area.

3. Exact computation

An exact calculation of the pseudo-power spectrum covariance matrix can be obtained by integrating Eq. (6). We propose an algorithm that performs the computation in $O(\ell_{\max}^5)$, typically gaining a thousandfold speed-up compared to the direct implementation in $O(\ell_{\max}^6)$. This is achieved with the fast harmonic transform tools implemented in the HEALPix library⁵. It enables the exact computation of the covariance matrix, albeit on a limited range of multipoles. In this work, we have computed the full covariance up to $\ell_{\max,\text{ex}} \equiv 1000$, and calculated a few ranks of the matrix at $\ell > \ell_{\max,\text{ex}}$. This allows the direct comparison of the various analytic covariance approximation formulae with the exact calculation.

In the following, we describe the algorithm we developed to perform this computation. We validate it with Monte Carlo estimates of the covariance for the reference SPT-3G survey.

3.1. Algorithm description

We focus on the computation of a given row of the covariance matrix $\tilde{\Sigma}$. This will allow us either to compute a full covariance matrix at low multipoles, or to test our approximations on a selection of rows. We first start by describing the computation of the covariance of the intensity spectrum. A diagrammatic implementation of our calculation is presented in Fig. 2. For the polarization spectra, the calculation follows a similar pattern, and the difference between the two cases will be discussed in the next section.

We describe in App. B the derivation of the expression of the covariance of the pseudo-spectrum leading to Eq. (6). In particular, we express the covariance as a sum over m and m' of the square of the correlation $\langle \tilde{a}_{\ell m} \tilde{a}_{\ell' m'}^* \rangle$

$$\tilde{\Sigma}_{\ell\ell'} = \frac{2}{(2\ell+1)(2\ell'+1)} \sum_{mm'} |\langle \tilde{a}_{\ell m} \tilde{a}_{\ell' m'}^* \rangle|^2. \quad (7)$$

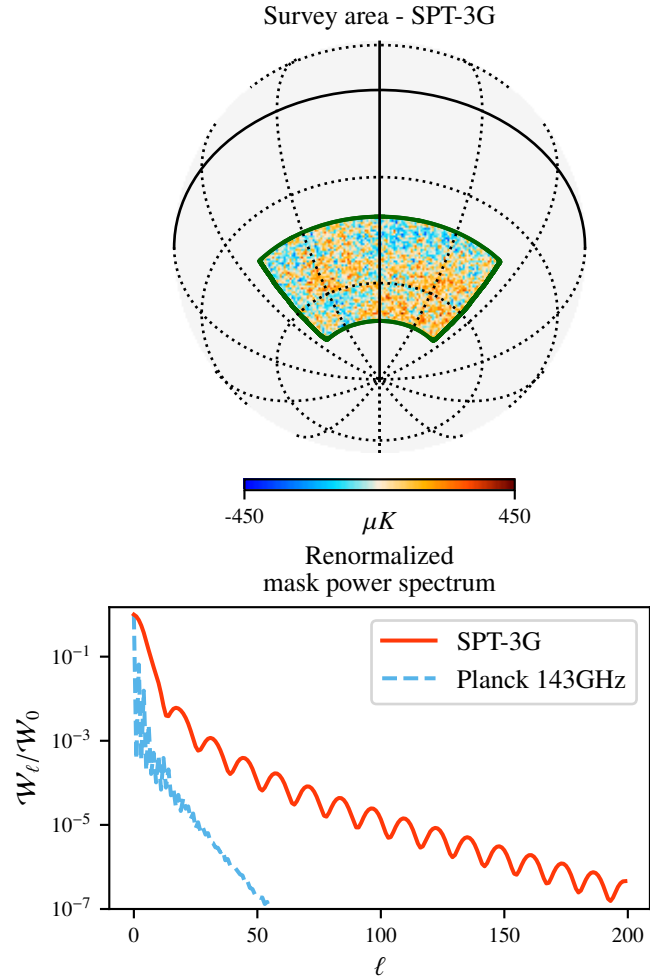


Fig. 1: Top: CMB temperature anisotropies on the SPT-3G patch in galactic coordinates. The dark green line delimits the survey footprint. The vertical and horizontal bold black lines are the zero-longitude and zero-latitude coordinates, respectively. The SPT-3G patch covers roughly 4% of the sky. Bottom: Mask power spectra as defined in Eq. (A.4) for SPT-3G and for the 143 GHz map used in the *Planck* cosmological analysis, which covers around 70% of the sky. The spectra have been renormalised by their first value for comparison purposes. Masks corresponding to small sky fractions, such as the SPT-3G one, have a shallower power spectrum compared to large ones.

⁵<https://healpix.sourceforge.io>

The harmonic coefficients correlation can be written as

$$\begin{aligned} \langle \tilde{a}_{\ell m} \tilde{a}_{\ell' m'}^* \rangle &= \sum_{LM} C_L {}_0 I_{\ell m LM} {}_0 I_{\ell' m' LM}^*, \\ &= \int d\hat{u} {}_0 Y_{\ell m}(\hat{u}) W(\hat{u}) \sum_{LM} \{C_L {}_0 I_{\ell' m' LM}^*\} {}_0 Y_{LM}^*(\hat{u}), \end{aligned} \quad (8)$$

where we have used Eq. (2) to expand one of the ${}_0 I$ kernels, re-organized the equation, and used the fact that the power spectrum C_L and the mask W are real quantities (we also dropped the explicit W dependencies of the kernel to simplify notations). For fixed ℓ' and m' , the rightmost part of the equation can be seen as the complex conjugate of the backward spherical harmonic transform of a set of spherical harmonic coefficients into a map

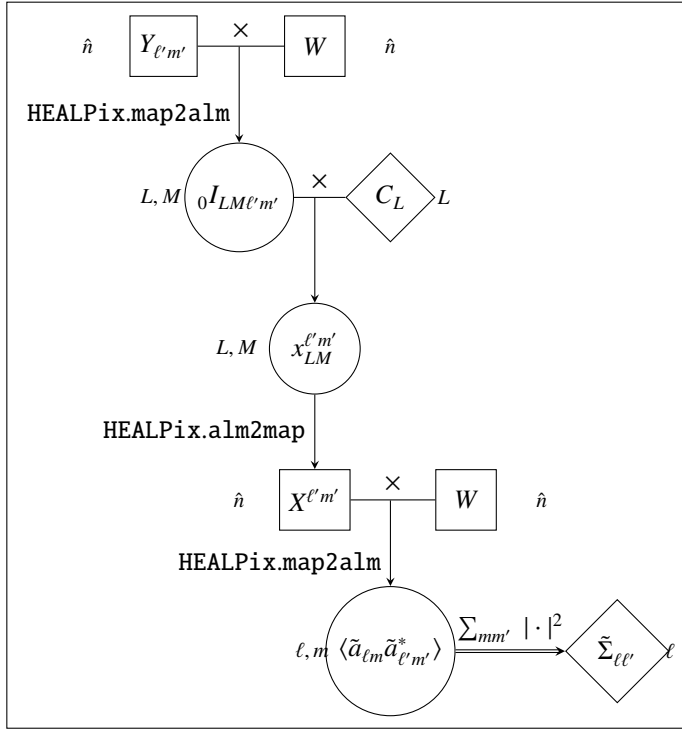


Fig. 2: Diagram showing the algorithm to compute one row of the covariance $\tilde{\Sigma}_{\ell\ell'}$ using the HEALPix tools for a fixed ℓ' and varying ℓ . Square, diamond or circle boxes are arrays representing maps, power spectra or spherical harmonic coefficients respectively. Operations are symbolized by arrows and described alongside. The indices of the arrays are indicated on the side of the corresponding boxes. For example, near the top of the diagram, the HEALPix.map2alm operation applied on the product $Y_{\ell' m'} W$ produces the array ${}_0 I_{LM' m'}$ with indices L, M . At the bottom of the diagram, the operations before the final summation produce the array $\langle \tilde{a}_{\ell m} \tilde{a}_{\ell' m'}^* \rangle$ with indices ℓ, m for a fixed ℓ', m' pair. This part of the algorithm scales as $O(\ell'^3)$, since this is the scaling of HEALPix operations (which we apply 3 times) when the resolution of the map is comparable to the maximum multipole index considered. The last operation, summing over the indices m, m' , requires repeating the precedent steps for all $m' \in [-\ell', \ell']$, thus repeating them $2\ell' + 1$ times. Therefore, the final complexity to produce a single row with fixed multipole index ℓ' is $O(\ell'^4)$. Computing the covariance matrix for all ℓ' then increases the computational time to $O(\ell'^5)$.

$X^{\ell' m'}$, defined as

$$X^{\ell' m'}(\hat{u}) \equiv \sum_{LM} x_{LM}^{\ell' m'} Y_{LM}(\hat{u}), \quad (9)$$

where we defined the spherical harmonic coefficients with

$$x_{LM}^{\ell' m'} \equiv C_L {}_0 I_{LM \ell' m'}^*. \quad (10)$$

Here, we emphasize that the map $X^{\ell' m'}$ is a complex map, thus it needs special care when decomposing into harmonic coefficients. With these definitions, Eq. (8) reduces to

$$\langle \tilde{a}_{\ell m} \tilde{a}_{\ell' m'}^* \rangle = \int d\hat{u} {}_0 Y_{\ell m}(\hat{u}) W(\hat{u}) X^{\ell' m'*}(\hat{u}), \quad (11)$$

where we recognize the forward harmonic transform of the map $X^{\ell' m'}$, masked by W . Thus, a spherical harmonic transform of a masked map can produce the correlation $\langle \tilde{a}_{\ell m} \tilde{a}_{\ell' m'}^* \rangle$ for all ℓ, m and a fixed pair of ℓ', m' . As we discussed, this $X^{\ell' m'}$ map is defined by a set of spherical harmonic coefficients whose expression is given in Eq. (10).

The computation of the $x_{LM}^{\ell' m'}$ coefficients requires the evaluation of the ${}_0 I$ kernel. Using Eq. (2) for a fixed ℓ', m' , the ${}_0 I_{LM \ell' m'}$ kernel can be computed as the spherical harmonic transform of a masked ${}_0 Y_{\ell' m'}$ map, for all of the L, M indices. Putting everything together, we see that for a choice of ℓ', m' , the computation of $\langle \tilde{a}_{\ell m} \tilde{a}_{\ell' m'}^* \rangle$ for all ℓ, m reduces to two forward and one backward spherical harmonic transforms, as summarized in Fig. 2.

In practice, these decompositions can be performed with HEALPix, which takes advantage of a specific pixelation scheme to make the computation more efficient. This is where the gain announced at the beginning of this section comes from and allows us to implement the exact computation. HEALPix decompositions typically scale as $O(\ell'^3)$ ⁶. We repeat the decompositions resulting in $\langle \tilde{a}_{\ell m} \tilde{a}_{\ell' m'}^* \rangle$ for all $m' \in [-\ell', \ell']$ to perform the summation in Eq. (7). Thus, the computation of a single rank $\tilde{\Sigma}_{\ell\ell'}$ for all ℓ and fixed ℓ' scales as $O(\ell'^4)$. Finally, the computation of a full covariance matrix for all ℓ' scales as $O(\ell'^5_{\max, \text{ex}})$.

Additional optimisations can be implemented in the algorithm, namely by degrading maps and running the algorithm at a lower HEALPix resolution, n_{side} , for small multipoles. HEALPix computations are precise up to $\ell \sim 2n_{\text{side}}$, hence choosing a map resolution of the order of the multipole is sufficient to compute precisely the close-to-diagonal elements of the covariance. This operation requires a degraded version of the mask, which must be computed while avoiding aliasing from small scale features. This can be done by implementing a hard cut-off of the mask harmonic coefficients before degrading its resolution. Doing so allowed us to compute the exact covariance up to multipole $\ell_{\max, \text{ex}} = 1000$. The algorithm requires 300h of CPU-time to compute a row of the intensity (TTTT) and polarization (EEEE) matrices at multipole $\ell = 950$ with map resolution $n_{\text{side}} = 1024$. It is also well suited to a potential GPU implementation, which could lead to more speed-ups.

3.2. Polarization

The polarized case is very similar to the intensity one detailed in the previous subsection. We only describe the EEEE case which gives a general template to the other polarization and temperature×polarization cases.

⁶Details about the computation scaling of HEALPix can be found on the website or in Gorski et al. (2005)

The polarized version of Eq. (8) is given by Eq. (6) of Challinor & Chon (2004) that writes

$$\langle \tilde{a}_{\ell m}^E \tilde{a}_{\ell' m'}^{E*} \rangle = \sum_{LM} [C_L^{EE} + I_{\ell m LM} + I_{\ell' m' LM}^* + C_L^{BB} - I_{\ell m LM} - I_{\ell' m' LM}^*], \quad (12)$$

where we defined the Hermitian coupling coefficients

$$\pm I_{\ell m LM} = \frac{1}{2} ({}_{+2}I_{\ell m LM} \pm {}_{-2}I_{\ell m LM}), \quad (13)$$

with the spin-weighted coupling coefficients ${}_{\pm 2}I$ defined as for intensity, see Eq. (2). Reordering the terms and doing the same operations as in the previous section, the final harmonic coefficient correlation can be seen as the masked forward spherical harmonic decomposition of two maps $Z_1^{\ell' m'}, Z_2^{\ell' m'}$,

$$\begin{aligned} \langle \tilde{a}_{\ell m}^E \tilde{a}_{\ell' m'}^{E*} \rangle &= \frac{1}{2} \left[\int d\hat{u} W(\hat{u}) Z_1^{\ell' m'}(\hat{u}) \left({}_{+2}Y_{\ell m}^* + {}_{-2}Y_{\ell m}^* \right) (\hat{u}) \right. \\ &\quad \left. - i \int d\hat{u} W(\hat{u}) Z_2^{\ell' m'}(\hat{u}) \left({}_{+2}Y_{\ell m}^* - {}_{-2}Y_{\ell m}^* \right) (\hat{u}) \right]. \end{aligned} \quad (14)$$

The maps $Z_1^{\ell' m'}, Z_2^{\ell' m'}$ are obtained using a backward spherical harmonic decomposition of the coefficients $x_{LM}^{\ell' m'; E, B}$,

$$(Z_1^{\ell' m'} - iZ_2^{\ell' m'})(\hat{u}) \equiv \sum_{LM} \frac{x_{LM}^{\ell' m'; E} + x_{LM}^{\ell' m'; B}}{2} {}_{+2}Y_{LM}(\hat{u}), \quad (15)$$

$$(Z_1^{\ell' m'} + iZ_2^{\ell' m'})(\hat{u}) \equiv \sum_{LM} \frac{x_{LM}^{\ell' m'; E} - x_{LM}^{\ell' m'; B}}{2} {}_{-2}Y_{LM}(\hat{u}). \quad (16)$$

The set of harmonic coefficients $x_{LM}^{E, B}$ are defined similarly to the temperature case (Eq. (10)), and obtained by filtering the coefficients computed with a masked forward harmonic decomposition of the spin-2 spherical harmonics ${}_{\pm 2}Y_{\ell' m'}$,

$$\begin{cases} x_{LM}^{\ell' m'; E} = C_L^{EE} + I_{\ell' m' LM}, \\ x_{LM}^{\ell' m'; B} = C_L^{BB} - I_{\ell' m' LM}. \end{cases} \quad (17)$$

This algorithm can be extended for any combination of spectra for the other polarization cases, including the cross-correlation between temperature and polarization that we don't treat here.

3.3. Validation on simulations

We compare the results of our implementation of the exact computation with a Monte-Carlo estimate of the covariance, obtained with N_{sim} simulations. The Monte-Carlo covariance terms are expected to be Wishart distributed with N_{sim} degrees of freedom, as explained in Lueker et al. (2010). We can estimate their variance to be

$$\langle \langle \tilde{\Sigma}_{\ell\ell'}^{\text{sim}} - \langle \tilde{\Sigma}_{\ell\ell'}^{\text{sim}} \rangle \rangle^2 \rangle = \frac{\tilde{\Sigma}_{\ell\ell'}^2 + \tilde{\Sigma}_{\ell\ell} \tilde{\Sigma}_{\ell'\ell'}}{N_{\text{sim}}}. \quad (18)$$

$N_{\text{sim}} = 10\,000$ allows us to reach a percent level accuracy on the diagonal. This is the number of realizations that we will use for the Monte-Carlo covariance. For this validation, we will use the mask shown in Fig. 1. Note that in this idealized setting, we do not include a point source mask.

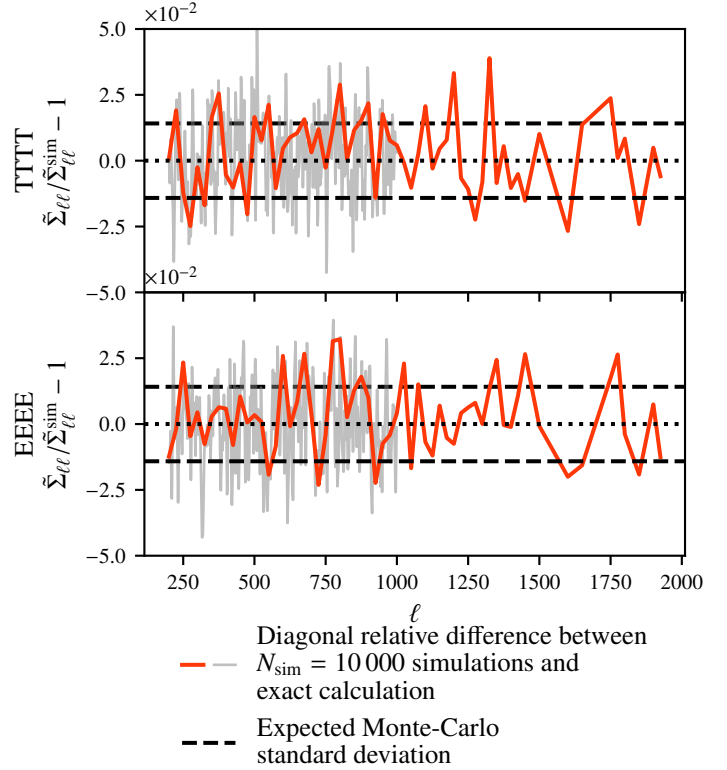


Fig. 3: Relative difference of diagonals $\tilde{\Sigma}_{\ell\ell}/\tilde{\Sigma}_{\ell\ell}^{\text{sim}} - 1$ for temperature TTTT (top) and polarization EEEE (bottom). In red are the relative differences every 25 multipoles until $\ell = 1500$ and a few well chosen ones (at the locations of peaks and troughs of the spectra) up to $\ell = 2000$. In grey, the same quantity is plotted for all multipoles for $\ell \in [\ell_{\text{cut}} = 200, \ell_{\text{max,ex}} = 1000]$. We are able to compute exactly the covariance only for a limited number of rows, and it is computationally cheaper for lower multipoles, justifying our choice of full calculation at $\ell < \ell_{\text{max,ex}}$ and partial calculation for larger multipoles. This plot shows the agreement between the two approaches, validating our exact calculation.

We perform an exact computation of the TTTT and EEEE covariance up to $\ell_{\text{max,ex}} = 1000$, using our algorithm and degrading the mask to smaller resolutions. Furthermore, we compute the rows every 25 multipoles of the matrix up to $\ell_{\text{max}} = 1500$, as well as at a few well chosen multipoles, corresponding to peaks and troughs of the spectra, up to $\ell_{\text{max}} = 2000$.

We first focus on the diagonal of the covariance. Figure 3 presents the comparison between the exact computation of the diagonal, obtained by selecting the corresponding value in the rows we have computed, and the MC evaluation. The two agree within the MC noise expected for N_{sim} .

For what concerns the off-diagonal terms, we show in Fig. 4 a few rows of the exact and Monte-Carlo covariance, which agree within MC noise. The correlation between modes falls to the percent level within a distance $|\ell - \ell'| \sim 25$ band around the diagonal. The correlation matrix is defined as the covariance renormalised by its diagonal

$$\sigma_{\ell\ell'} \equiv \frac{\Sigma_{\ell\ell'}}{\sqrt{\Sigma_{\ell\ell} \Sigma_{\ell'\ell'}}}. \quad (19)$$

We display the exact and Monte-Carlo correlation matrix on the same multipole range in Fig. 5.

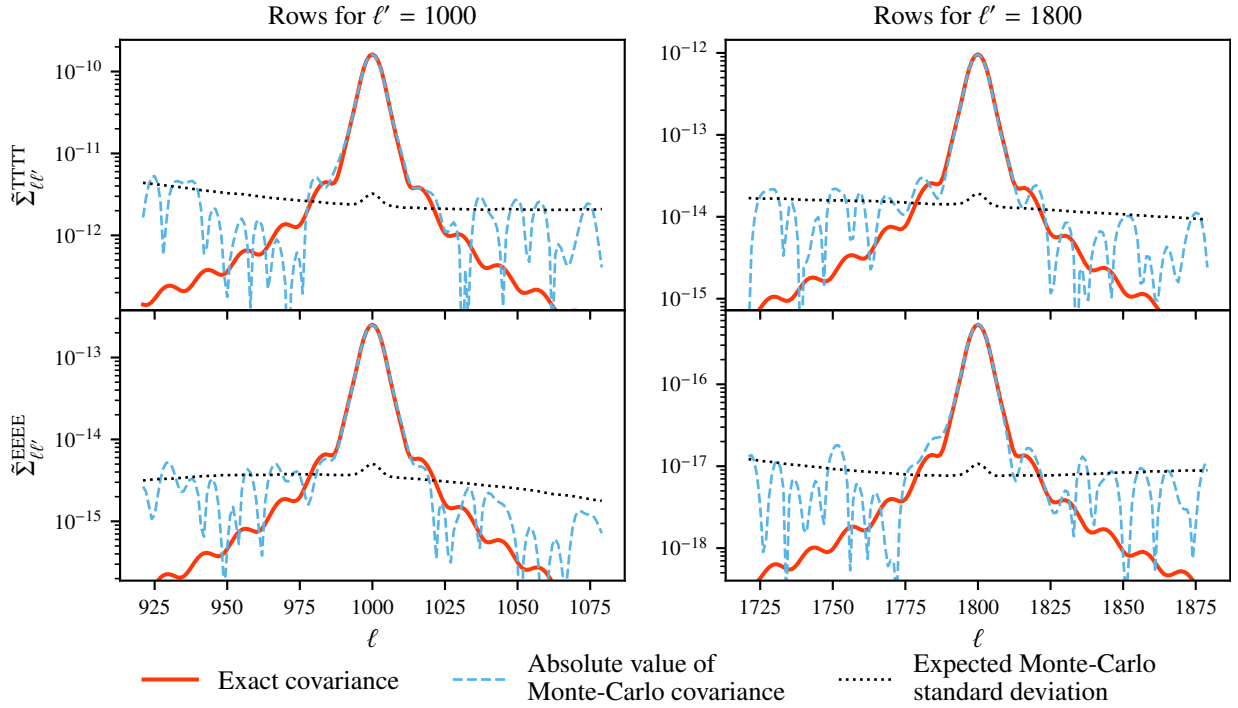


Fig. 4: Rows of the exact covariance (solid red) and of the simulated one (dash blue), for multipole $\ell' = 1000$ (left hand side) and $\ell' = 1800$ (right hand side). The dotted black line shows the expected Monte-Carlo uncertainty on the simulated covariance from Eq. (18), using $N_{\text{sim}} = 10\,000$ realizations. There is excellent agreement between the two approaches. The Monte-Carlo standard deviation is as large as the covariance off-diagonal terms at $|\ell - \ell'| \sim 25$.

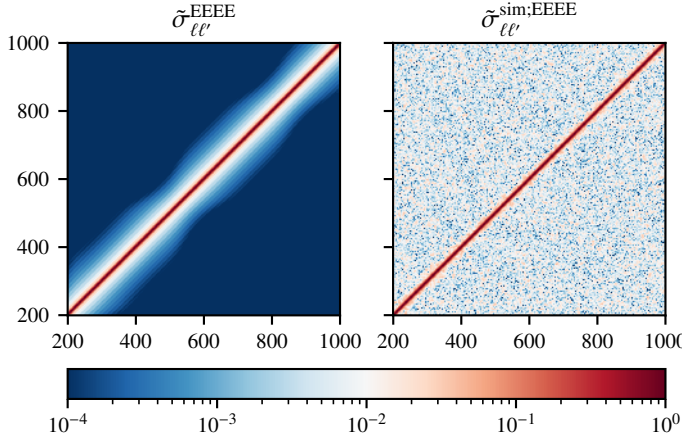


Fig. 5: EEEE correlation matrix (see Eq. (19)) obtained from the exact (left) and Monte-Carlo (right) calculations of the covariance matrix. The exact computation allows us to have the full correlation matrix, whilst the Monte-Carlo approach is limited by numerical noise. All terms below 10^{-4} are plotted in dark blue.

While massive Monte-Carlo estimates, as we performed here in this idealized case, can produce accurate off diagonal terms estimates, performing a large number of Monte-Carlo can be more challenging in the case of a realistic experiment, requiring regularization approaches, where the number of possible simulations is limited by the computational cost of mock-observations.

We also stress that our covariance matrix cannot be directly compared to the one used in Dutcher et al. (2021), since the presence of a point source mask (that we did not include in our sim-

ple example), the complications brought about by introducing realistic noise and scanning strategy, projection effects (the analysis in Dutcher et al. (2021) is performed using a flat sky approach) can all yield to different levels of correlations between modes.

Our tests demonstrate that our implementation of the exact computation of the pseudo-spectrum covariance is correct, at least at the level of accuracy that can be reached by Monte-Carlo estimation.

4. Existing approximations and their accuracy on a small patch of the sky

Our algorithm allows us to obtain the exact covariance only for $\ell < 1000$ or for a few rows at higher ℓ 's, due to the expensive computing resources required. The usual analytical approach consists in using approximations of Eq. (6) to decrease the computational cost. In this section, we introduce a new framework to express the approximations of the covariance matrix and use it to list the different methods proposed in the literature. Then, we test and discuss their accuracy against our exact computation.

4.1. General framework

Before discussing the approximations of the covariance, we define a few quantities that help relate the various approximations to each other. We rewrite Eq. (6) as

$$\tilde{\Sigma}_{\ell\ell'} = \frac{2}{(2\ell + 1)(2\ell' + 1)} \sum_{\ell_1 \ell_2} C_{\ell_1} \Theta_{\ell\ell'}^{\ell_1 \ell_2} [W] C_{\ell_2}, \quad (20)$$

introducing $\Theta_{\ell\ell'}^{\ell_1 \ell_2} [W]$, the *covariance coupling kernel*, defined as the sum over the multipole orders (m, m', \dots) of the coupling

coefficients reads

$$\Theta_{\ell\ell'}^{\ell_1\ell_2}[W] \equiv \sum_{mm_1m'm_2} ({}_0I_{\ell m\ell_1m_1} {}_0I_{\ell_1m_1\ell'm'} {}_0I_{\ell'm'\ell_2m_2} {}_0I_{\ell_2m_2\ell m})[W]. \quad (21)$$

The covariance coupling kernel Θ represents the coupling between the modes of the theoretical underlying power spectrum C_{ℓ_i} for $i = 1, 2$ depending on the index of the pseudo-covariance (ℓ, ℓ') . We chose to show the two indices related to the covariance (ℓ, ℓ') as subscripts, and the two summing indices (ℓ_1, ℓ_2) as superscripts. In this work, we consider a single-mask temperature case, for which the coupling kernel is symmetric with respect to the exchange of multipole indices $\ell \leftrightarrow \ell'$ or $\ell_1 \leftrightarrow \ell_2$. In the following, we will write our results in this case for the sake of simplicity, but they are valid regardless of the choice of single or multiple masks. In the case of spectra obtained from maps with different masks, or the case of cross-spectra, the kernel is not symmetric. While the results of this work apply to both cases, considering multiple masks increases computing cost.

Using the closing relations of spherical harmonics, given in Eqs. (A.10) and (A.11), we can write,

$$\sum_{\ell_1\ell_2} \Theta_{\ell\ell'}^{\ell_1\ell_2}[W] = (2\ell + 1)(2\ell' + 1)\Xi_{\ell\ell'}^{00}[W^2]. \quad (22)$$

We can now define the *reduced covariance coupling kernel* as

$$\bar{\Theta}_{\ell\ell'}^{\ell_1\ell_2}[W] \equiv \frac{\Theta_{\ell\ell'}^{\ell_1\ell_2}[W]}{(2\ell + 1)(2\ell' + 1)\Xi_{\ell\ell'}^{00}[W^2]}, \quad (23)$$

for which

$$\sum_{\ell_1\ell_2} \bar{\Theta}_{\ell\ell'}^{\ell_1\ell_2}[W] = 1. \quad (24)$$

With these notations, one can rewrite the covariance as

$$\tilde{\Sigma}_{\ell\ell'} = 2\Xi_{\ell\ell'}^{00}[W^2] \sum_{\ell_1\ell_2} C_{\ell_1} \bar{\Theta}_{\ell\ell'}^{\ell_1\ell_2}[W] C_{\ell_2}. \quad (25)$$

The symmetric mode-coupling kernel $\Xi[W^2]$ provides the purely geometric coupling due to sky masking and is common to all approximations of the covariance. It only depends on the power spectrum of the squared mask. Its computation scales as $O(\ell_{\max}^3)$. This could be improved by noting, as was done by Louis et al. (2020), that at small enough scales, $\Xi[W^2]$ is close to a Toeplitz matrix allowing us to further reduce the scaling to $O(\ell_{\max}^2)$ for a large range of modes. The sum on the right hand-side of Eq. (25) describes the contribution of the signal power spectrum modulated by the kernel Θ , which depends on the mask. It is this sum that all approximations try to simplify, replacing the kernel Θ with a simpler ansatz. In the following, we will describe all approximations in terms of this redefinition of the covariance matrix.

4.2. Approximations

4.2.1. NKA

Based on the observation that the coupling coefficients ${}_0I$ in Eq. (1) are narrow and peaking at their first multipole indices ℓ or ℓ' , Efstathiou (2004) introduced the following approximation of Eq. (25), taking the convolving spectra C_{ℓ_i} , $i = 1, 2$ out of the sum, and replacing them by the power spectrum evaluated at the

first multipole index of the coupling coefficients (*i.e.* the covariance indices of $\bar{\Theta}$), C_{ℓ} or $C_{\ell'}$. Following the notation introduced in García-García et al. (2019), we will refer to this approximation of the covariance as NKA (Narrow Kernel Approximation).

$$\begin{aligned} \tilde{\Sigma}_{\ell\ell'} &\approx 2C_{\ell}C_{\ell'}\Xi_{\ell\ell'}^{00}[W^2] \sum_{\ell_1\ell_2} \bar{\Theta}_{\ell\ell'}^{\ell_1\ell_2}[W] \\ &= 2C_{\ell}C_{\ell'}\Xi_{\ell\ell'}^{00}[W^2] \equiv \tilde{\Sigma}_{\ell\ell'}^{\text{NKA}}. \end{aligned} \quad (26)$$

In terms of the reduced covariance coupling kernel, the NKA approximation uses

$$\bar{\Theta}_{\ell\ell'}^{\ell_1\ell_2}[W] \approx \bar{\Theta}_{\ell\ell'}^{\ell_1\ell_2;\text{NKA}}[W] \equiv \frac{\delta_{\ell\ell_1}\delta_{\ell'\ell_2} + \delta_{\ell'\ell_1}\delta_{\ell\ell_2}}{2}. \quad (27)$$

The approximation is exact for the full sky or for a constant underlying power spectrum $C_{\ell} = N$. It provides an accurate estimator whenever the underlying power spectrum C_{ℓ} varies slowly as a function of ℓ compared to the typical size of the operators ${}_0I$. This condition is fulfilled when the amplitude of the mask power spectrum drops quickly with multipole ℓ , which is the case for large sky fractions observed with a mask which contains no small scale features. This is shown for example in Fig. 1, where we plot the power spectrum of one of the masks used in the *Planck* analysis. In this case, the above approximation holds for multipoles much larger than those for which the mask spectrum contains power.

The NKA approximation was first introduced in intensity by Efstathiou (2004) and extended to polarization in Challinor & Chon (2004). As in the temperature case, the approximated covariances in polarization are expressed as a function of the polarization spectra EE and BB and the symmetric coupling kernels $\Xi_{\ell\ell'}^{\pm 2, \pm 2}$. The expressions of the approximated polarization covariances mix EE and BB due to leakage which appears because the sky is masked, see Eq. (25-27) of Challinor & Chon (2004).

The NKA approximation has been widely used, for instance in the *Planck* cosmological analysis, which masked only small portions of the full sky, see Planck Collaboration et al. (2015). However, it has never been thoroughly tested on small sky fractions. As shown in Fig. 1, the mask power spectrum in the case of the small survey footprint of SPT-3G drops much slower than the large *Planck* one. From this observation, we expect the mode coupling kernels ${}_0I$ to be wider, as it can be deduced from Eq. 2. As a result, the theoretical underlying spectrum C_{ℓ} might not be treated as constant compared to the covariance coupling kernels in the sums of Eq. (25), and SPT-3G may be outside the regime of validity of the NKA assumption. This will be tested at the end of this section. We will now list some proposed improvements to the NKA approximation.

4.2.2. FRI

A straightforward extension of the NKA approximation has been proposed in Friedrich et al. (2021). It is based on the observation that the reduced covariance coupling kernel $\bar{\Theta}$ has four maxima at $[\ell = \ell_1, \ell' = \ell_1]$, $[\ell = \ell_1, \ell' = \ell_2]$, $[\ell = \ell_2, \ell' = \ell_1]$ and $[\ell = \ell_2, \ell' = \ell_2]$. This suggests the following form of the reduced covariance coupling matrix:

$$\bar{\Theta}_{\ell\ell'}^{\ell_1\ell_2}[W] \approx \bar{\Theta}_{\ell\ell'}^{\ell_1\ell_2;\text{FRI}}[W] \equiv \frac{\delta_{\ell\ell_1} + \delta_{\ell'\ell_1}}{2} \frac{\delta_{\ell\ell_2} + \delta_{\ell'\ell_2}}{2}. \quad (28)$$

Thus, the approximated covariance is

$$\tilde{\Sigma}_{\ell\ell'}^{\text{FRI}} \equiv 2\Xi_{\ell\ell'}^{00}[W^2] \left(\frac{C_{\ell} + C_{\ell'}}{2} \right)^2. \quad (29)$$

We will refer to this approximation as FRI in the rest of the article.

4.2.3. INKA

Nicola et al. (2021) proposed an improved version of the NKA, the INKA (Improved Narrow Kernel Approximation). In this approximation, the Dirac functions in Eq. (27) are replaced by ${}_0\bar{M}$, the renormalised MASTER mode-coupling kernel, as defined in App. A.3. It writes

$$\bar{\Theta}_{\ell\ell'}^{\ell_1\ell_2}[W] \approx \bar{\Theta}_{\ell\ell'}^{\ell_1\ell_2;\text{INKA}}[W] \equiv \frac{{}^0\bar{M}_{\ell\ell_10}\bar{M}_{\ell'\ell_2} + {}^0\bar{M}_{\ell'\ell_10}\bar{M}_{\ell\ell_2}}{2}. \quad (30)$$

Indeed, the convolution in Eq. (6) averages the power spectra C_{ℓ_i} , $i = 1, 2$ over multipoles close to ℓ and ℓ' . One can take advantage of this by replacing the convolution by a multiplication with a smoothed power spectrum. If one defines $\bar{C} \equiv \bar{M}C$, the resulting covariance can be written as

$$\tilde{\Sigma}_{\ell\ell'}^{\text{INKA}} \equiv 2\bar{C}_{\ell}\bar{C}_{\ell'}\Xi_{\ell\ell'}^{00}[W^2]. \quad (31)$$

All the NKA, FRI and INKA scale as $O(\ell_{\text{max}}^3)$, which are the computing resources needed to obtain the coupling kernels Ξ and \bar{M} . This is a significant improvement over the $O(\ell_{\text{max}}^6)$ scaling of the full computation. We will now turn to validating the approximations in the case of small surveys, using the expensive exact computation of the covariance matrix.

4.3. Accuracy

We test the accuracy of the NKA, FRI and INKA approximations using the exact computation in the case of the SPT-3G small survey footprint shown in Fig. 1. For this mask, the correlations between modes are significant, as already seen in Fig. 4. In this case, it is customary to bin the individual multipoles into wider bandpowers. For this reason, we will perform all of our tests on a binned version of the covariance. Given the shape of the power spectrum of the mask and the correlations that we expect from it, we adopt a $\Delta\ell = 50$ binning with $\ell(\ell+1)/(2\pi)$ weights to flatten the dynamics of the spectra in each bin. With this bin size, we expect that most of the correlations between bandpowers are concentrated in the first off-diagonal bin. We will also conservatively exclude the first $\ell_{\text{cut}} = 200$ multipoles from our analysis. Those are more challenging to measure on small survey footprint as they can suffer from leakage from the super survey scales. We will restrict our comparison to the multipoles between ℓ_{cut} and $\ell_{\text{max,ex}} = 1000$, where we have carried out the exact computation of all of the matrix rows.

We present in Fig. 6 a comparison between the exact computation and the NKA, FRI and INKA approximations, for the diagonal and first off-diagonal of the TTTT and EEEE binned covariances. We will discuss the performance of our new ACC approximation, also shown in the figure, later in the next section. The existing approximations provide good estimates of those elements of the covariance as they fall within 5% of accuracy. The amplitude of the errors vary at different multipoles. Even though the FRI and INKA schemes were implemented to improve upon the simple NKA approximation, their errors are of similar amplitude for this choice of binning. However, all approximations fail to recover the binned covariance at the percent level. In Sect. 5, we will use the knowledge gained from the exact computation to propose an improved approximation scheme.

At higher multipoles, since we cannot easily compute the full matrix to present binned results, we only compare some unbinned rows in Fig. 7. The shaded regions in this figure give the worst values of the relative difference for the approximation within multipoles $\ell \in [\ell_{\text{cut}} = 200, \ell_{\text{max,ex}} = 1000]$ and $\ell' \in [\ell - 2\Delta\ell, \ell + 2\Delta\ell]$. Those are the covariance terms for which we can calculate the full binned covariance, and whose accuracy is shown in Fig. 6. Furthermore, the lines in Fig. 7 show the same quantity as the shaded regions, *i.e.* the maximal relative difference, but for multipoles $\ell \in [\ell_{\text{max,ex}}, 2000]$, estimated over the sparse number of rows for which we have computed the matrix exactly. We see that the difference with the exact covariance for all approximations at large multipoles are always within the same error range as for lower multipoles. This shows that the approximations still work with the same precision at higher multipoles, both for temperature and polarization and that the accuracy of the approximations in the unbinned case quickly falls below 20% when $\Delta = 50$.

4.4. Structure of the reduced covariance coupling kernel

Our expression of the covariance matrix approximations in terms of the normalized coupling kernel $\bar{\Theta}$ in Eq. (27) gives us a very efficient tool for examining the validity of each approximation and better understand their differences. We designed an algorithm to calculate this kernel exactly similar to the one described in Sect. 3 for the exact calculation of the matrix. We show a diagram of the algorithm in Fig. 8.

The reduced covariance coupling kernel is then displayed in Fig. 9 for the INKA, NKA and FRI approximations compared to the exact computation for a fiducial multipole $\ell = 200$. The kernels are represented as matrices as a function of ℓ_1, ℓ_2 , for different fixed choices of the indices ℓ, ℓ' . Columns show the results for different choices of $\ell' = \ell - \Delta$, with $\Delta = 0$ (*i.e.* the kernels for the diagonal terms of the covariance matrix, *e.g.* $\tilde{\Sigma}_{200,200}$), or $\Delta = 10, 50$ (*i.e.* the kernels for the off-diagonal terms separated by 10 or 50 multipoles, *e.g.* $\tilde{\Sigma}_{200,190}$). We remind the reader that the reduced kernel is multiplied to C_{ℓ_1}, C_{ℓ_2} and summed over the indices ℓ_1, ℓ_2 in Eq. (25). Hence, Fig. 9 directly shows the weight of the ℓ_1, ℓ_2 power spectra which contribute to the $\tilde{\Sigma}_{\ell\ell'}$ element of the covariance matrix.

We first focus on the kernels for the diagonal of the covariance matrix, $\Delta = 0$, shown on the first column of Fig. 9. All kernels peak at $\ell_1 = \ell_2 = \ell$, as expected. However, it is clear from the exact calculation that the kernel has a significant width compared to the CMB power spectrum. This is more clearly shown in Fig. 10, where we plot a slice of the coupling kernels for $\ell_1 = 200$. One can see that the width of the kernel cannot be neglected compared to the slope of the CMB power spectrum. This justifies the INKA approximation, which replaces the Dirac δ functions of NKA and FRI by renormalised mode coupling kernels, *see* Eq. (31). However, as shown in this figure, the INKA kernel is slightly larger compared to the exact calculation and of smaller amplitude. This explains why INKA underestimates the covariance diagonal in the peaks of the power spectrum and overestimates it on the troughs, as shown in Fig. 6, since it averages the underlying power spectrum in a larger range of multipoles. Conversely, the NKA/FRI kernels are much thinner compared to exact computation, and so they overestimate the diagonal in the peaks and underestimate it in the troughs of the power spectrum.

Second, we focus on the off-diagonal terms, $\Delta = 10, 50$, shown in the second and third column of Fig. 9. The difference between the exact computation and all of the existing approxi-

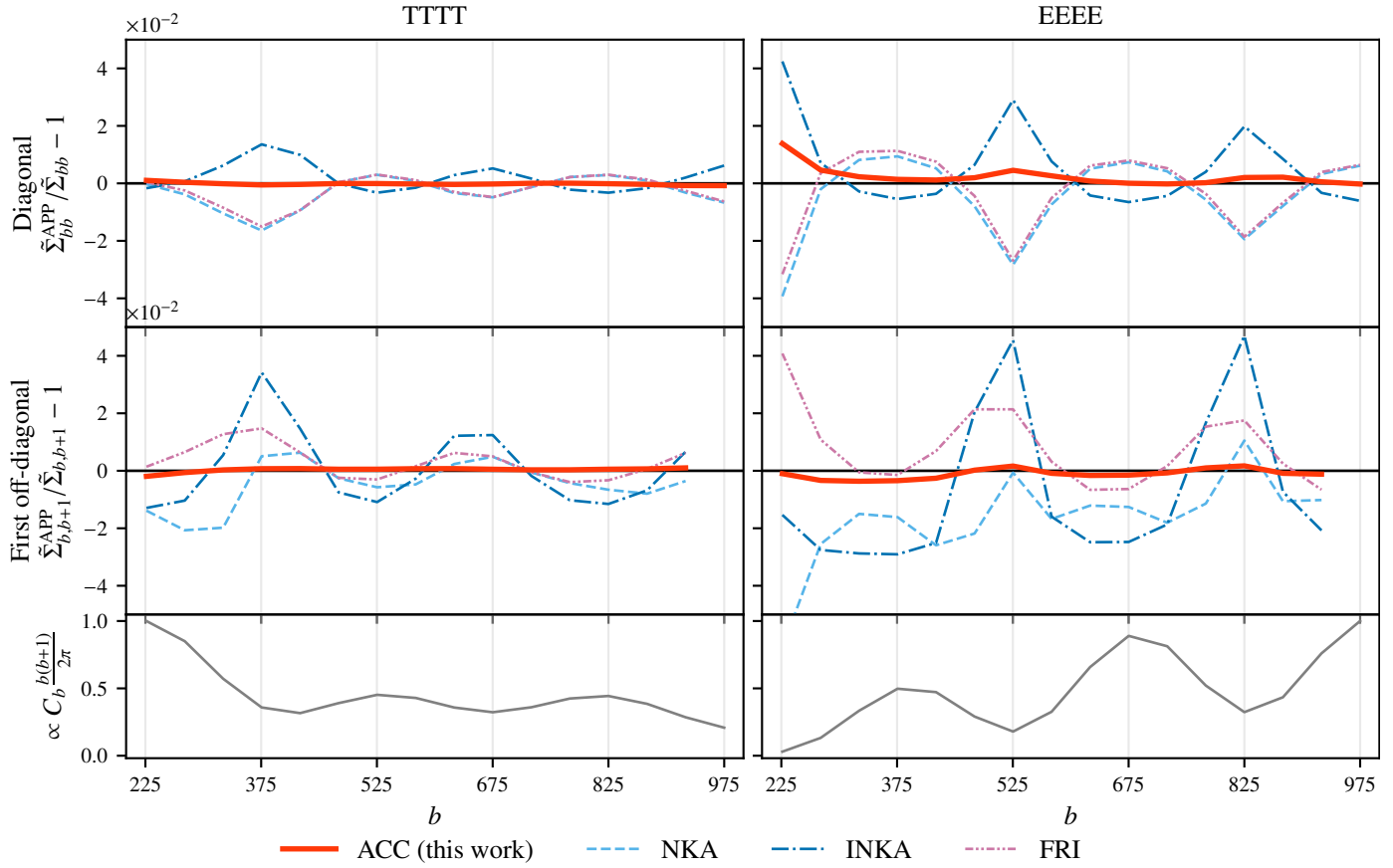


Fig. 6: Relative differences of binned approximations with respect to the exact binned covariance: $\tilde{\Sigma}_{bb'}^{\text{APP}} / \tilde{\Sigma}_{bb'} - 1$, for TTTT (left hand side) and EEEE (right hand side), with binning $\Delta\ell = 50$. On the first row are plotted the relative differences for the diagonal, *i.e.* $b = b'$, while on the second row are plotted those of the first off-diagonal, *i.e.* $b' = b + 1$. The NKA (light blue dash), FRI (purple dash-double-dot) and INKA (dark blue dash-dot) approximations are accurate at the 5% level, whereas the ACC approximation (solid red) reaches the 1% level, both in intensity and polarization for multipoles larger than $\ell_{\text{cut}} = 200$. The relative differences are plotted for bins that include multipoles up to $\ell_{\text{max,ex}} = 1000$ since it is the maximum multipole for which we have computed all the rows of the exact covariance. The third row displays the corresponding binned underlying renormalised spectrum TT or EE, to put forward that the difference on the covariances are on the peaks and troughs of the spectra, since this is where the correlation between adjacent scales will have the most impact.

mations is striking and it is clear that the kernel has more structure than the simple approximated forms. For close off-diagonal terms such as $\Delta = 10$, the true kernel peaks at its central index $\ell_1 = \ell_2 = \bar{\ell} \equiv (\ell + \ell')/2$. For far off-diagonal terms such as $\Delta = 50$, there are four maxima as predicted by the FRI approximation, which are partially missed by the INKA approximation. Moreover, the true coupling has more dynamics and covers also negative values. This is the reason why the different approximations, even the INKA one, fail to correctly represent the off-diagonal terms of the covariance, as observed in Fig. 7.

5. A new approximation for the covariance

5.1. Improved Approach: the Approximated Covariance Coupling (ACC)

Our ability to calculate the exact reduced covariance coupling matrix $\bar{\Theta}$, described in Section 4, allows us to introduce a new approximation for the computation of the pseudo-power spectrum covariance matrix. Indeed, we notice that for a fixed $\Delta = \ell' - \ell$, the structure of $\bar{\Theta}_{\ell\ell'}$ seems invariant. In other words, the coupling matrices contributing to the $\tilde{\Sigma}_{\ell\ell'}$ term of the covariance matrix only depend on the distance Δ from the diagonal. This is

demonstrated in Fig. 11, where we plot diagonal and slices of the exact calculation of $\bar{\Theta}_{\ell,\ell+\Delta}$ for $\Delta = 50$ and different ℓ , for $\ell_1 = \ell$. The plot reveals that the kernels are nearly identical when plotted as a function of $\Delta_2 = \ell_2 - \ell$. We thus infer that in general if one writes the $\bar{\Theta}$ matrices as a function of $\Delta_1 = \ell_1 - \ell$ and $\Delta_2 = \ell_2 - \ell$, these only depend on $\Delta = \ell' - \ell$, for any ℓ and ℓ' . The difference between kernels computed at different ℓ 's for same Δ is small, at the 5% percent level. We can thus assume that for any choice of multipole ℓ, λ :

$$\forall (\ell, \lambda), \bar{\Theta}_{\ell(\ell+\Delta)}^{(\ell+\Delta_1)(\ell+\Delta_2)} \approx \bar{\Theta}_{\lambda(\lambda+\Delta)}^{(\lambda+\Delta_1)(\lambda+\Delta_2)}. \quad (32)$$

An analytical justification of this approximation is provided in App. E using the asymptotic expansion of the Wigner-3j symbols when ℓ is large.

This suggests a new approximation where the coupling kernel just has to be computed at a given fiducial ℓ for all relevant values of Δ, Δ_1 and Δ_2 . We will denote this new *approximated covariance coupling* method as ACC. More precisely, the ACC kernel is given by

$$\bar{\Theta}_{\ell\ell'}^{\ell_1\ell_2} \approx \bar{\Theta}_{\ell(\ell+\Delta); \text{ACC}}^{(\ell+\Delta_1)(\ell+\Delta_2)} \equiv \bar{\Theta}_{\ell^*(\ell^*+\Delta)}^{(\ell^*+\Delta_1)(\ell^*+\Delta_2)}, \quad (33)$$

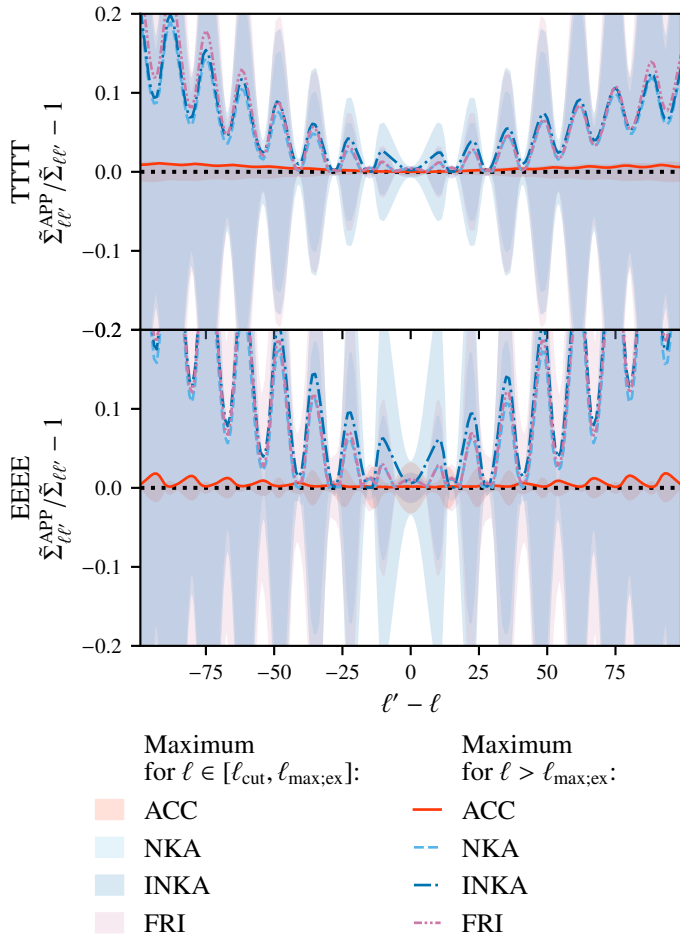


Fig. 7: Relative difference between the unbinned approximated covariance matrices compared to the exact calculation, $\tilde{\Sigma}_{\ell\ell'}^{\text{APP}} / \tilde{\Sigma}_{\ell\ell'} - 1$, as a function of $\Delta = \ell - \ell'$. We show the NKA (light blue), INKA (dark blue) and FRI (purple) approximations for TTTT (top) and EEEE (bottom). We only show the relative differences for the ℓ at which the deviation is largest, with $\ell \in [\ell_{\text{cut}}, \ell_{\text{max,ex}}]$ (shaded regions) or $\ell \in [\ell_{\text{max,ex}}, 2000]$ (lines). By comparing the two, one can see that the approximations perform with a similar level of accuracy at low and high- ℓ . For comparison, we also plot our new approximation ACC (red), which we will introduce in Sect. 5. The ACC approximation improves over the others by a factor of ~ 4 .

where we perform the exact and costly computation only for the $\bar{\Theta}_{\ell_1 \ell_2}^{(\ell^* + \Delta_1)(\ell^* + \Delta_2)}$. We are free to choose the reference ℓ^* multipole. Since there are no significant long range correlations in our case, we can pick a low⁷ ℓ^* and use a low n_{side} map resolution. We have to make sure, however, that ℓ^* is larger than ℓ_{cut} , the low- ℓ cutoff that was introduced to avoid issues with large scale leakages. Close to ℓ_{cut} , the exact computation can be used. Note that with a small mask, large scale modes are difficult to measure and usually excluded from the cosmological analysis. We can also restrict the range of Δ to the number of off-diagonal terms of interest in the covariance matrix. The correlation falls quickly (see Figs. 4 and 5) and, in practice, we can restrict it to $|\Delta| < d_{\text{max}}$, with d_{max} being of the order of a few times the correlation length. Similarly, the kernels fall quickly in Δ_1, Δ_2 , so

⁷in the limit where the asymptotic justification of App. E remains valid.

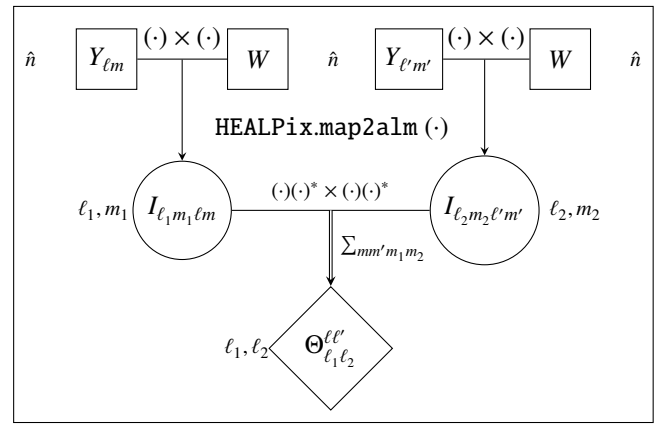


Fig. 8: Diagram showing the algorithm to compute the reduced covariance coupling kernels using HEALPix tools. We use the same notation as in the diagram of Fig. 2. The HEALPix functions require $O(n_{\text{side}}^3)$, with n_{side} the chosen resolution of maps W and $Y_{\ell m}$. As we choose the resolution n_{side} to be of the order of the multipoles indices ℓ, ℓ' , it is equivalent to say that they require $O((\ell + \ell')^3)$. As operations are done $O(\ell + \ell')$ times, the whole operation of computing $\bar{\Theta}_{\ell\ell'}$ is $O((\ell + \ell')^4)$. Finally, it is clear in this diagram that the computing time of this kernel is at least doubled if one uses multiple masks. One would have different masks as inputs in the first line. As a result, one would have to compute the coupling coefficients for each of the masks, as shown in Eq. (D.3).

we can also restrict ourselves to a small region of a similar order and, in the case of the single mask analysis, use the symmetry around $\Delta \leftrightarrow -\Delta$ to reduce the cost of the computation.

While we only presented temperature coupling kernels in Fig. 9, the situation is identical in polarization, and a similar approximation can be built, see App. E. We used this approximation with $\ell^* = 300$, $n_{\text{side}} = 512$ and $d_{\text{max}} = 100$ to compute the ACC results in Fig. 6.

5.2. Accuracy and scaling

We validate the accuracy of our ACC approximation and compare it to the other approximations in Fig. 6. Our new approximation succeeds at estimating the covariance within 1% error for all multipoles larger than ℓ_{cut} , in intensity and polarization, which is a factor of ~ 4 improvement over previous approximations. This is also shown in Fig. 7 and in Fig. 12, which is just the same as Fig. 7 but focused on the EEEE ACC residuals with respect to INKA. It is clear from this figure that the ACC approximation estimates much better both the diagonal and off-diagonal terms of the covariance matrix.

Figure 8 shows the computations needed to obtain the covariance coupling kernels. Following the same argumentation as for the exact computation of the Sect. 3, we can show that the computation of a single kernel $\bar{\Theta}$ scales as $O((\ell + \ell')^4)$. As a result, since we need to compute one for each diagonal index $\Delta \in [0, d_{\text{max}}]$, the final ACC approximation scales as $O(n_{\text{side}}^4 d_{\text{max}})$, where n_{side} is the map resolution chosen to compute the kernels. The computing resources needed to obtain $\bar{\Theta}$ for all approximations are summarized in Table 1. They add up to the resources needed to compute the symmetric coupling kernel Ξ in Eq. 25. In practice, the kernel \bar{M} needed to build INKA is often already known for the sky analysis, as it has the same structure as Ξ , so the effective complexity for this approximation is $O(1)$.

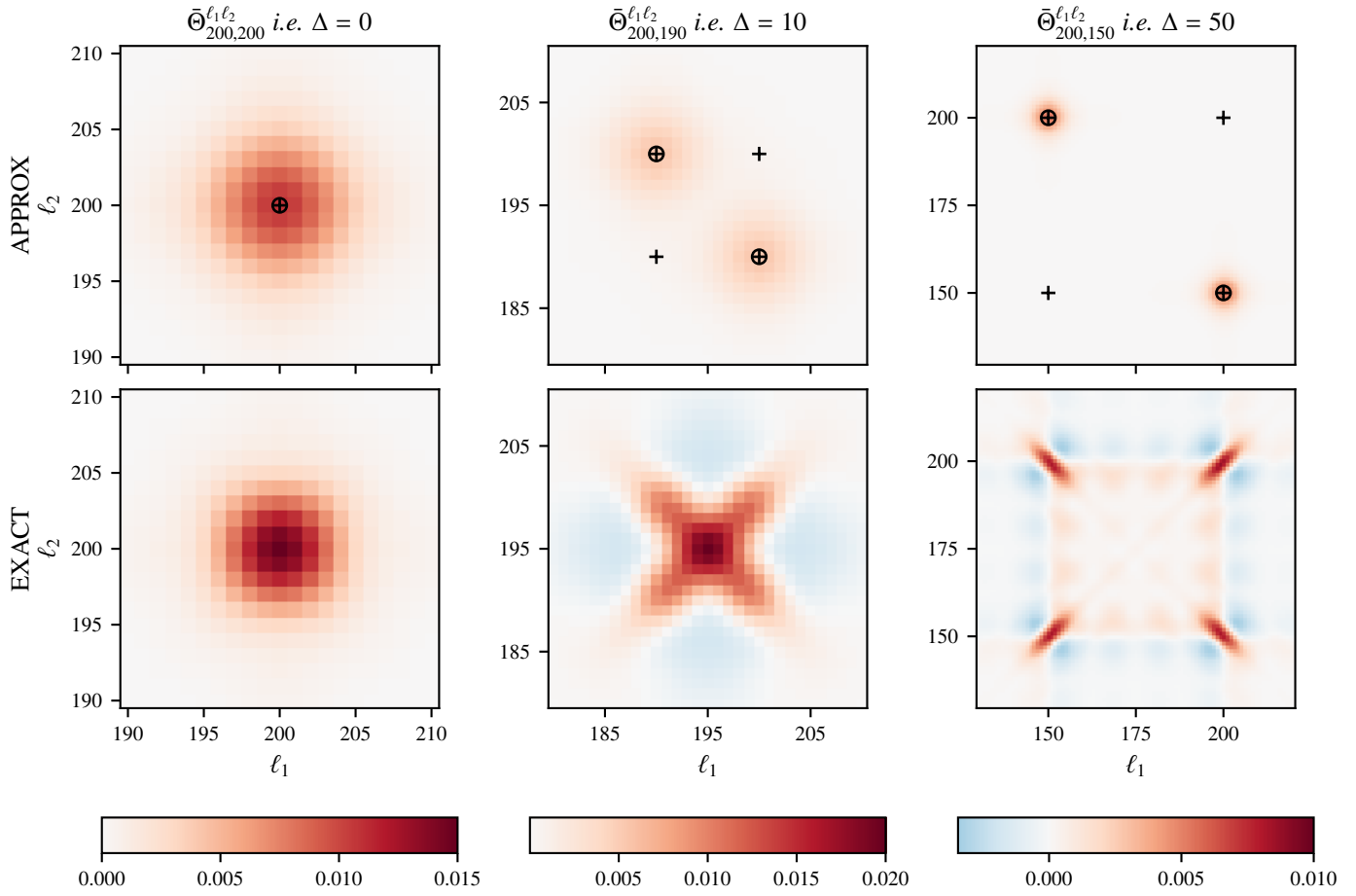


Fig. 9: Reduced covariance coupling kernels $\bar{\Theta}_{\ell\ell'}^{\ell_1\ell_2}$ for $\ell = 200$ and $\ell' = \ell + \Delta$, with $\Delta = [0, 10, 50]$ shown in the three different columns. All kernels in one column share the same colormap. All of the matrices are shown as a function of ℓ_1 and ℓ_2 and are centered in $\ell_1, \ell_2 = (\ell + \ell')/2$. Each of the displayed kernels is properly normalized according to Eq. (22). The plots are restricted to the elements which have a significant value. The top row shows the approximated INKA kernels and the positions where the delta distributions of the NKA (circles) and FRI (crosses) approximation peak. The bottom row shows the exact kernels. The comparison between the two highlights how much of the structure of the exact kernel is missed by the different approximations.

Method	Mathematical definition	$\bar{\Theta}_{\ell\ell'}^{\ell_1\ell_2}$	Precision	Complexity
Exact (this work)	25	$\bar{\Theta}_{\ell\ell'}^{\ell_1\ell_2}$ computed $\forall \ell, \ell', \ell_1, \ell_2$	N/A	$O(\ell_{\max}^5)$ (using HEALPix pixelation)
NKA	26	$(\delta_{\ell\ell_1}\delta_{\ell'\ell_2} + \delta_{\ell'\ell_1}\delta_{\ell\ell_2})/2$	4%	$O(1)$
FRI	29	$(\delta_{\ell\ell_1} + \delta_{\ell'\ell_1})(\delta_{\ell\ell_2} + \delta_{\ell'\ell_2})/4$	4%	$O(1)$
INKA	31	$(_0\bar{M}_{\ell\ell_1 0}\bar{M}_{\ell'\ell_2} + _0\bar{M}_{\ell'\ell_1 0}\bar{M}_{\ell\ell_2})/2$	4%	$O(\ell_{\max}^3)$ or $O(\ell_{\max}^2)$ with Louis et al. (2020)
ACC (this work)	33	$\bar{\Theta}_{\ell\ell'}^{\ell_1\ell_2}$ invariant for $\Delta \equiv \ell - \ell' = \text{cst}$	1%	$O(d_{\max} n_{\text{side}}^4)$

Table 1: Summary of computation methods to obtain the pseudo-power spectrum covariance matrix. First column: Name of approximation. Second column: Equation to which they are referred. Third column: Expression of $\bar{\Theta}$ in this approximation. Fourth column: Precision determined by the maximum values of the relative difference of the EEEE binned covariance on diagonal for multipoles $\ell_{\text{cut}} \leq \ell \leq \ell_{\max, \text{ex}}$ in Fig. 6. For larger multipoles, the approximation are expected to be in this range of precision as shown in Fig. 12. Fifth column: Summary of computing resources needed to obtain $\bar{\Theta}$ in each approximation. Let us here specify that for INKA, the kernel \bar{M} is often already known, thus the practical complexity is $O(1)$. ℓ_{\max} is the multipole range of the covariance, d_{\max} is the number of diagonal computed in the ACC approximation, n_{side} is the resolution chosen to compute the covariance coupling kernels in the ACC approximation (closest to ℓ_{cut} is sufficient).

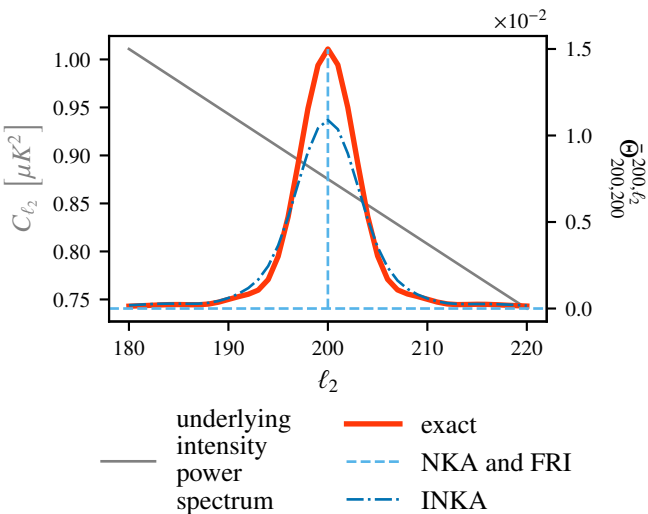


Fig. 10: Slices of the exact covariance coupling kernel (solid red) versus the approximated NKA/FRI (dash light blue) and INKA (dot-dash dark blue) ones (right hand side scale). We show for comparison the CMB intensity power spectrum (left hand side scale, solid gray line). The typical width of the exact coupling kernel for a small sky footprint is large enough that the power spectrum cannot be considered as nearly constant, as required by the NKA/FRI approximations. The INKA kernel is lower than the exact one at the maximum but have larger tails. This explains why the INKA covariance mainly deviates on the peaks or troughs of the power spectrum, where it underestimates or overestimates (respectively) the convolution of the kernel with the power spectrum.

5.3. Point source mask

We did not include a point source mask in the survey footprint. Point source masks significantly complicate the problem as the power spectrum of the mask will have power at large multipoles, hence it will extend the correlation length. This has been an issue for all analyses thus far. Apodizing the point source masks helps to alleviate the problem but at the price of discarding a significant area of the usable sky. Even in the case of a large survey footprint, such as *Planck*, the point source masks have been shown to break the NKA approximation. In this case the issue was mitigated using a simulation-based correction. Concerning FRI, INKA and ACC, preliminary work that we have performed also suggest that they fail when including sources. We expect these approximations to perform poorly since the improvements over NKA are focused on the central shape of the reduced covariance coupling matrix $\tilde{\Theta}$, while the sources tend to affect the far off-diagonal terms, increasing the correlation between distant multipoles. Looking particularly at the ACC approximation, the larger correlations at distant multipoles will break the asymptotic behavior of the Wigner-3j symbols shown in App. E. We can expect that this will reduce the validity of the approximated invariance by translation along the covariance diagonal, which is at the core of the ACC approximation. More work is required to assess the accuracy of ACC and other approximations in this case. However, one can adopt different approaches to mitigate the effect of a point source mask. For example, one could find analytical solutions (Gratton et al. (2022), in prep.), inpaint the maps (Benoit-Lévy et al. 2013), or use a Monte-Carlo correction such as the one used in *Planck* (Planck Collaboration et al. 2015).

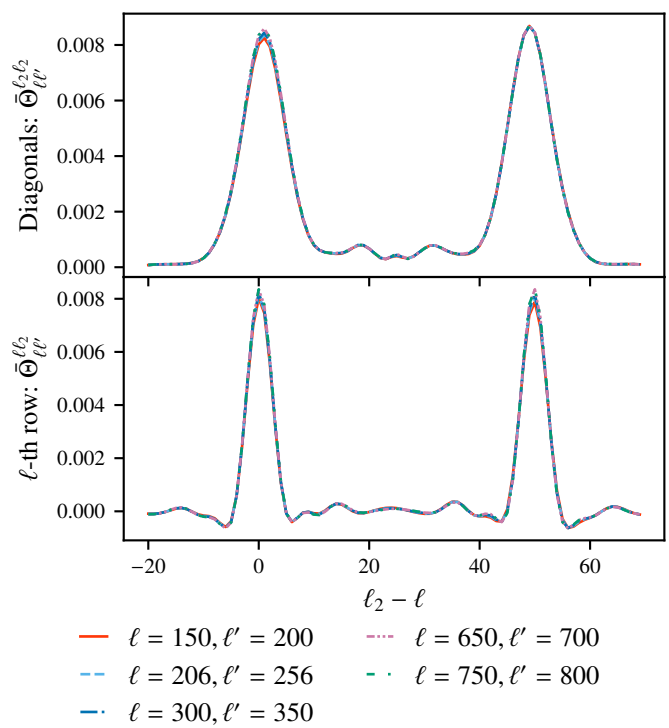


Fig. 11: Slices of the reduced covariance coupling kernels $\bar{\Theta}_{\ell,\ell'}^{\ell_1,\ell_2}$ for $\ell \in [150, 206, 300, 650, 750]$, $\Delta = \ell' - \ell = 50$ and $\Delta_1 = \ell_1 - \ell = 0$, as a function of $\Delta_2 = \ell_2 - \ell$. The plots show that for different ℓ but same Δ , the kernels are very similar, differing only at the 5% level. A similar result can be shown for other values of Δ . This leads us to formulate our new approximation, where we assume $\bar{\Theta}$ to depend only on the multipole separations $\Delta, \Delta_1, \Delta_2$.

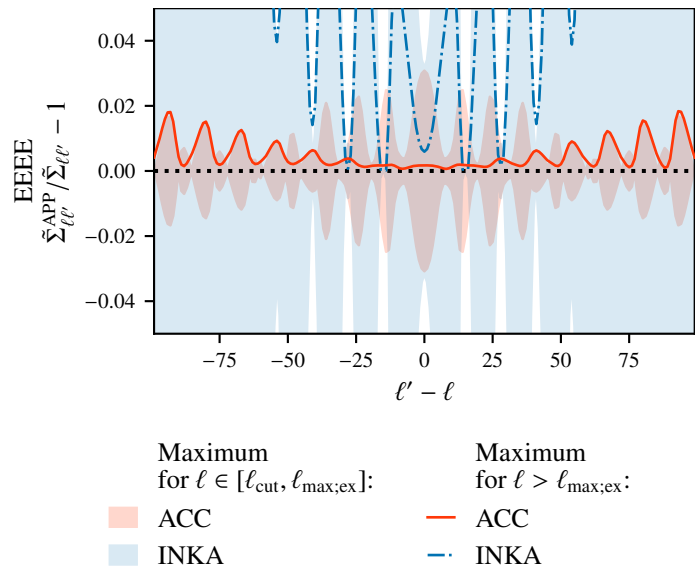


Fig. 12: Zoom of Fig. 7. We focus on the relative differences of the ACC and INKA covariance matrices with respect to the exact covariance for EEEE. The deviations found at $\ell < 1000$ (shaded regions) are similar to the ones found at the higher multipoles (lines), showing that the approximations work at the same level of accuracy in the two cases.

6. Covariance of the PolSpice estimator

The pseudo-power spectrum is a biased estimator of the true underlying spectrum of the masked CMB maps. To recover an unbiased estimator, one can apply the MASTER (Hivon et al. 2002) formalism, which inverts the mode-coupling matrix and applies it to the biased estimator. Similarly, one can use the PolSpice (Szapudi et al. 2001; Chon et al. 2004) algorithm, which corrects the two point correlation function for the effect of the mask in real space and then converts the result back into harmonic space. However, when the sky footprint is small, and large angular scales are not observed, the unbinned mode-coupling matrix becomes non-invertible. Analogously, the PolSpice conversion of the two-point correlation function into a power spectrum cannot be performed. In the first case, the mode-coupling matrix must be binned to allow the inversion. In the second case, one must apodize (i.e. gradually cut) the large angular scales of the two-point correlation function before calculating the corresponding power spectrum. This introduces a small bias in the final estimator which cannot be corrected for.

In this section, we will explain in detail how to calculate the covariance matrix for the PolSpice estimator starting from a pseudo-power spectrum covariance matrix, which we will produce through our ACC approximation. We will show how to include the effect of the correction of the mask, as well as the small bias introduced by the PolSpice apodization of the two-point correlation function. In particular, we will show that this apodization can be expressed in harmonic space, allowing us to relate the PolSpice spectrum covariance matrix to the the pseudo-spectrum one with a convolution.

6.1. MASTER equation

The pseudo-power spectrum is related to the true one through the well-known MASTER equation introduced in Hivon et al. (2002)

$$\langle \tilde{C}_\ell^{\text{TT}} \rangle = \sum_{\ell'} {}_0M_{\ell\ell'} C_{\ell'}^{\text{TT}}, \quad (34)$$

with similar equations for polarization, see App. A.2. This bias comes from the missing information due to the masked sky. Given the weighted mask $W(\hat{n})$, one can compute ${}_0M$ using Eq. (A.15). Provided that ${}_0M$ is invertible, an unbiased estimator can be constructed. These relations can be expressed in real space using the two-point correlation functions ξ , which for a statistically isotropic sky depend only on the relative angle between two directions

$$\langle T(\hat{n}_1)T(\hat{n}_2) \rangle = \xi(\arccos(\hat{n}_1 \cdot \hat{n}_2)). \quad (35)$$

They can be related to the power spectrum C_ℓ using a Legendre series, with

$$\xi(\theta) = \sum_{\ell} \frac{2\ell+1}{4\pi} C_\ell P_\ell(\cos \theta), \quad (36)$$

$$C_\ell = 2\pi \int_0^\pi d\cos \theta \xi(\theta) P_\ell(\cos \theta). \quad (37)$$

If we define in the same manner the correlation function $\tilde{\xi}$ of the masked sky, associated with the pseudo-spectrum \tilde{C}_ℓ , we obtain from Eq. (34), by applying the decomposition in a Legendre series, the following relation

$$\langle \tilde{\xi}(\theta) \rangle = w(\theta) \xi(\theta), \quad \forall \theta \in [0, \pi], \quad (38)$$

where $w(\theta)$ is the mask angular correlation function (more details can be found in App. C). From this relation, we can establish that the MASTER mode-coupling matrix ${}_0M$ is invertible only if the correlation function of the mask $w(\theta)$ is non-zero for all $\theta \in [0, \pi]$, which implies that the survey area explores all angular separations on the sky. While this is valid for almost full sky analyses such as the *Planck* one, it does not hold for experiments observing small patches, such as SPT-3G, where angular scales larger than $\theta \sim 30$ deg are unexplored. As a result, ${}_0M$ is not invertible. Binning allows the regularization of the MASTER matrix and thus to build a nearly-unbiased estimator of the bandpowers. This approach is described in Hivon et al. (2002) and is adopted in NaMaster⁸ (Alonso et al. 2019). Similarly, we show in the next section how the unobserved large angular scales are handled in the PolSpice estimator.

6.2. Regularizing with PolSpice

6.2.1. Temperature

The pseudo-power spectrum estimator can be regularized in real space following the PolSpice approach in Szapudi et al. (2001). The pseudo-correlation function $\tilde{\xi}$ is smoothed with a scalar apodizing function $f^{\text{apo}}(\theta)$, which cuts out large θ , and then corrected for the bias coming from the weighted mask described in Eq. (38). The scalar apodizing function goes smoothly from $f^{\text{apo}}(0) = 1$ to $f^{\text{apo}}(\theta_{\max}) = 0$ to avoid Fourier ringing. θ_{\max} should be chosen as the maximal angular size of the weighted mask. A new correlation function estimator $\hat{\xi}(\theta)$ is defined as

$$\hat{\xi}(\theta) \equiv g(\theta) \tilde{\xi}(\theta), \quad (39)$$

with

$$g(\theta) = \begin{cases} f^{\text{apo}}(\theta)/w(\theta) & \forall \theta \in [0, \theta_{\max}], \\ 0 & \forall \theta \in [\theta_{\max}, \pi]. \end{cases} \quad (40)$$

The function g is well defined and smooth for all angles thanks to the apodization f^{apo} . As a consequence of Eq. (38) and Eq. (39), the PolSpice estimator of the correlation function can be related on average to the true underlying correlation function with

$$\langle \hat{\xi}(\theta) \rangle = f^{\text{apo}}(\theta) \xi(\theta) \quad \forall \theta \in [0, \pi]. \quad (41)$$

Going back to harmonic space using a Legendre transform, this operation can be expressed as:

$$\langle \hat{C}_\ell \rangle = \sum_{\ell'} {}_0K_{\ell\ell'} C_{\ell'} \quad (42)$$

$${}_0K_{\ell\ell'} = (2\ell' + 1) \Xi_{\ell\ell'}^{00} [f^{\text{apo}}] \quad (43)$$

The PolSpice kernel ${}_0K$ is obtained from the scalar apodizing function f^{apo} with an extended definition of the operators Ξ (see App. C and Eq. (C.7) for more details). The operator acts on the Legendre transform of f^{apo} .

The advantage of PolSpice, which performs the regularization in real space rather than in harmonic space, is that it replaces an ℓ -space convolution by an integration and a multiplication, which are faster and numerically more stable, producing an estimator for all multipoles ℓ . We will denote this estimator with a hat, for instance \hat{C}_ℓ^{XY} . Note that this regularization (which is only required for small sky patches) introduces a bias in the PolSpice estimator that cannot be corrected for. The bias is small, since ${}_0K$ is properly normalized, i.e. $\sum_{\ell\ell'} {}_0K_{\ell\ell'} = 1$.

⁸<https://github.com/LSSTDESC/NaMaster>

Furthermore, the regularization increases the correlations between unbinned modes. The PolSpice kernels behave as window functions, mixing multipoles of the pseudo-power spectrum. The lack of information at large scale induces the inability to distinguish multipoles which are close to each other. For this reason, for cosmological analyses, the spectrum estimator is binned in ranges larger than the typical correlation between multipoles.

6.2.2. Polarization

PolSpice allows one to correct for the bias introduced by the cut sky in the same manner for the polarized spectra. It also allows one to decouple the EE and BB estimator, see Challinor & Chon (2004) or the appendix of this work for details, App. C. Similarly to the intensity case, we can express the effect of the PolSpice real space regularization in spherical harmonics by defining the polarized PolSpice kernels: ${}_{\pm 2}K_{\ell\ell'} = (2\ell' + 1)\Xi_{\ell\ell'}^{2\pm 2}[f^{\text{apo}}]$. The PolSpice estimator follows for $X \in [\text{E}, \text{B}]$

$$\langle \hat{C}_{\ell}^{XX} \rangle = \sum_{\ell'} {}_{-2}K_{\ell\ell'} C_{\ell'}^{XX}. \quad (44)$$

Concerning the temperature×polarization case, we can show that

$$\langle \hat{C}_{\ell}^{\text{TE}} \rangle = \sum_{\ell'} {}_{\times}K_{\ell\ell'} C_{\ell'}^{\text{TE}}, \quad (45)$$

$$\text{with } {}_{\times}K_{\ell\ell'} = (2\ell' + 1)\Xi_{\ell\ell'}^{20}[f^{\text{apo}}]. \quad (46)$$

6.3. Relating PolSpice and MASTER in harmonic space

We can translate the relations Eq. (39) into harmonic space in temperature and polarization to obtain the PolSpice estimator as a harmonic convolution of the pseudo-power spectrum estimator

$$\hat{C}_{\ell}^{\text{TT}} = \sum_{\ell'} {}_0G_{\ell\ell'} \tilde{C}_{\ell'}^{\text{TT}}, \quad (47)$$

$$\hat{C}_{\ell}^{\text{EE}} - \hat{C}_{\ell}^{\text{BB}} = \sum_{\ell'} {}_{-2}G_{\ell\ell'} (\tilde{C}_{\ell'}^{\text{EE}} - \tilde{C}_{\ell'}^{\text{BB}}). \quad (48)$$

$$\hat{C}_{\ell}^{\text{EE}} + \hat{C}_{\ell}^{\text{BB}} = \sum_{\ell'} {}_{\text{dec}}G_{\ell\ell'} (\tilde{C}_{\ell'}^{\text{EE}} + \tilde{C}_{\ell'}^{\text{BB}}), \quad (49)$$

$$\hat{C}_{\ell}^{\text{TE}} = \sum_{\ell'} {}_{\times}G_{\ell\ell'} \tilde{C}_{\ell'}^{\text{TE}}. \quad (50)$$

The G kernels are constructed in the same manner as the PolSpice kernels, with the operator Ξ acting on the function $g = f^{\text{apo}}/w$ accordingly to Eq. (C.7) (or equivalently on the associated power spectrum of g via Legendre transform). They are given by

$${}_0G_{\ell\ell'} = (2\ell' + 1)\Xi_{\ell\ell'}^{00}[g], \quad (51)$$

$${}_{-2}G_{\ell\ell'} = (2\ell' + 1)\Xi_{\ell\ell'}^{2-2}[g], \quad (52)$$

$${}_{\times}G_{\ell\ell'} = (2\ell' + 1)\Xi_{\ell\ell'}^{20}[g], \quad (53)$$

$${}_{\text{dec}}G_{\ell\ell'} = \frac{2\ell' + 1}{2} \int_{-1}^1 g(\theta) d_{22}^{\ell}(\theta) d_{2-2}^{\ell'}(\theta) d\cos(\theta). \quad (54)$$

The first three equations above reduce to the inverse of the master kernels when the PolSpice apodization function is set to 1, *i.e.* no apodization. The last kernel, referred to as *dec* is the kernel that allows the decoupling of the EE and BB spectra. The appendix C gives more details on this point. ${}_{\text{dec}}G$ is associated

with integral relations in real space, thus its harmonic expression is not straightforward. This expression requires more numerical resources to be computed since there is no closed relations for the Wigner d-matrix with different multipole indices. It can be obtained with PolSpice for all ℓ , setting as input $\tilde{C}_{\ell'}^{\text{EE}} = \tilde{C}_{\ell'}^{\text{BB}} = \delta_{\ell\ell'}$.

6.4. Covariance of PolSpice estimator

Given the previous relations in Eq. (47), (48), (49) and (50), the covariance of the PolSpice estimator can be written as a convolution of the covariance of the pseudo-power spectrum, with

$$\begin{aligned} \hat{\Sigma}_{\ell\ell'}^{\text{TTTT}} &\equiv \text{cov}(\hat{C}_{\ell}^{\text{TT}}, \hat{C}_{\ell'}^{\text{TT}}) \\ &= \sum_{LL'} {}_0G_{LL'} \tilde{\Sigma}_{LL'}^{\text{TTTT}} {}_0G_{L'L'}. \end{aligned} \quad (55)$$

For polarization, there is mixing between the EE and BB components in the covariance. Let us write down the polarized EEEE PolSpice covariance, after defining ${}_{\pm}G \equiv \frac{1}{2}({}_{\text{dec}}G \pm {}_{-2}G)$, as

$$\begin{aligned} \hat{\Sigma}_{\ell\ell'}^{\text{EEEE}} &= {}_+G \tilde{\Sigma}_{\ell\ell'}^{\text{EEEE}} {}_+G^{\top} + {}_-G \tilde{\Sigma}_{\ell\ell'}^{\text{BBEE}} {}_+G^{\top} \\ &\quad + {}_+G \tilde{\Sigma}_{\ell\ell'}^{\text{EEBB}} {}_-G^{\top} + {}_-G \tilde{\Sigma}_{\ell\ell'}^{\text{BBBB}} {}_-G^{\top}. \end{aligned} \quad (56)$$

The polarized PolSpice covariance is built on the polarized pseudo-covariance, mixing the components EE and BB, thanks to the kernel ${}_{\pm}G$, see Fig. 13. This figure displays a row of the kernels computed on the mask SPT-3G used in our analysis. It shows the window functions that are applied to the pseudo-power spectra to produce the PolSpice spectra. The PolSpice apodizing function of the correlation function we used is:

$$f^{\text{apo}}(\theta) = \begin{cases} \frac{1}{2} \left(1 + \cos \frac{\pi\theta}{\theta_{\text{max}}} \right) & \forall \theta < \theta_{\text{max}}, \\ 0 & \text{otherwise.} \end{cases} \quad (57)$$

Here we have, $\theta_{\text{max}} = \pi/6$. Without apodization but with partial sky, as for *Planck*, the decoupling kernel ${}_{\text{dec}}G$ is not null, still resulting in a non-zero ${}_-G$ kernel. However, it will be orders of magnitude smaller than ${}_+G$, hence one can compute EEEE ignoring the leakage from covariance terms that include BB.

6.5. Accuracy of the covariance approximations for the PolSpice estimator

We can build estimates of the PolSpice spectrum covariance convolving the pseudo-spectrum covariance with the appropriate kernels following Eqs. (55) and (56). To calculate the pseudo-spectrum covariance, we can use the NKA, INKA, FRI and ACC approximations or the exact computation. Fig. 14 shows the accuracy of the binned PolSpice covariance calculated with the approximations compared to the exact calculation. The results are similar to the ones we found for the accuracy of the pseudo-spectrum covariances shown in Fig. 6. The NKA, INKA, FRI approaches provide a good estimate of the PolSpice covariance. However, the ACC approach improves dramatically over the existing approximations. This shows that our results for the accuracy of the pseudo-covariance holds also for the PolSpice one.

7. Summary and conclusions

One of the key ingredients of cosmological analyses based on power spectra are covariance matrices. Accurate covariance matrices ensure precise error bars and an unbiased estimation of

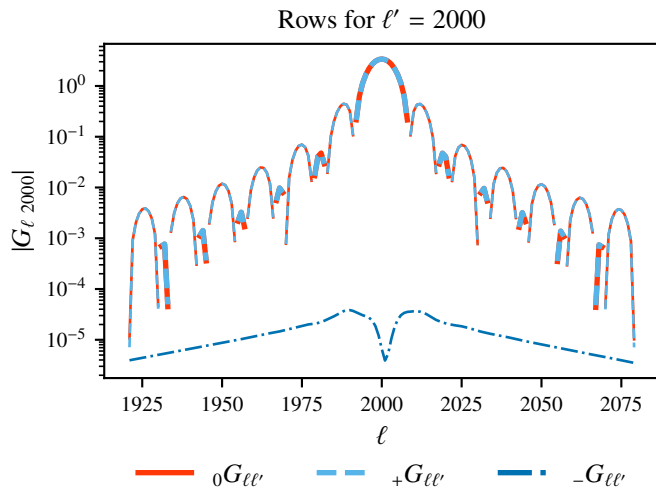


Fig. 13: Amplitude of the PolSpice convolution kernels G for the SPT-3G footprint. The negative terms are plotted with thinner lines. The kernels behave as window functions, mixing multipoles of the pseudo-power spectrum into the new PolSpice spectrum. They correct for the bias due to the mask, but introduce a small bias due to the lack of information at large scales. The temperature kernel ${}_0G$ and the polarization ${}_+G$ one are almost identical. The leakage kernel $_-G$ (all negative), which accounts for the mixing of the E and B polarization pseudo-spectra in the PolSpice spectrum, is orders of magnitudes smaller than the other two. Hence the BB covariance terms do not affect the EEEE covariance. On the other hand, the EE terms affect the BBBB covariance, as the EE spectrum is a few orders of magnitude larger than BB.

cosmological parameters. The analytical estimation of these matrices can be difficult in the case of small observed sky fractions, since existing approximations might fail. We have considered the specific example of estimating accurate analytical covariance matrices for the SPT-3G CMB experiment, whose survey covers around 4%, without masking the contribution of point sources. We considered both the cases of estimating the matrix for pseudo-power spectrum and for the PolSpice power spectrum estimator.

First, in Sec. 3, we implemented for the first time an expensive exact calculation of the covariance of the pseudo-power spectrum in intensity and polarization. We used a map-based algorithm that is accelerated thanks to the HEALPix pixelation tools. We were thus able to compute exactly the entire covariance matrix up to $\ell_{\max, \text{ex}} = 1000$. We also obtained a selection of rows of the covariance of particular interest up to $\ell = 2000$.

Thanks to this result, we were able to estimate precisely the accuracy of the existing approximations in Sec. 4 by comparing them to the binned exact covariances of the pseudo-power spectra measured on the SPT-3G patch. The approximations were found to be precise to the 5% level.

Then, using the code we developed for an exact computation of the covariance matrix, we estimated the covariance coupling kernel $\bar{\Theta}$, which determines how the CMB power spectrum couples into the covariance matrix. We were able to understand why the existing approximations in the literature fail to achieve a precision better than 5%. We then proposed in Sect. 5 a new approximation, the *Approximated Covariance Coupling* (ACC), which is more computationally expensive than the existing ap-

proximations, but allows one to have a more precise estimation of the covariance matrix at the 1% percent level.

Finally, in Sec. 6, we showed that we were able to build the covariance of the PolSpice power spectrum in both temperature and polarization using a harmonic correction. This computation is exact and based on the PolSpice algorithm real space corrections which we translated into harmonic space. Thanks to this correction, we produced estimates of the PolSpice covariance matrix based on the previous approximations of the pseudo-power spectrum covariance. The accuracy of the resulting PolSpice covariance approximations is the same as the pseudo-power spectrum case.

While this paper considered the particular example of the SPT-3G experiment, the results can be extended to non-CMB power spectrum analysis such as the one of weak shear or photometric catalogs. Also, we would like to stress that the accuracy of any of the approximations presented in this paper (existing or new one) is reduced once a point source mask is included in the sky footprint. Nevertheless, the exact computation of the covariance matrices still holds in this particular case. While previous experiments have included the effect of point source masks through the use of simulations (see e.g. [Planck Collaboration et al. \(2015\)](#)) or by inpainting the holes with constrained realizations (see e.g. [Benoit-Lévy et al. \(2013\)](#)), additional work is required to find an analytical calculation of this contribution.

Acknowledgements. We are grateful to the SPT collaboration for discussions and suggestions. We thank Lennart Balkenhol for discussions and insightful comments on the manuscript. This work has received funding from the French Centre National d'Etudes Spatiales (CNES). This project has received funding from the European Research Council (ERC) under the European Union's Horizon 2020 research and innovation programme (grant agreement No 101001897).

References

- Abazajian, K. N., Adshead, P., Ahmed, Z., et al., CMB-S4 Science Book, First Edition. 2016, arXiv e-prints, [1610.02743](#)
- Ade, P., Aguirre, J., Ahmed, Z., et al., The Simons Observatory: science goals and forecasts. 2019, *J. Cosmology Astropart. Phys.*, 2, 056, [1808.07445](#)
- Aghanim, N. et al., Planck 2018 results. V. CMB power spectra and likelihoods. 2020, *Astron. Astrophys.*, 641, [1907.12875](#)
- Aiola, S. et al., The Atacama Cosmology Telescope: DR4 Maps and Cosmological Parameters. 2020, *JCAP*, 12, 047, [2007.07288](#)
- Alonso, D., Sanchez, J., & Slosar, A., A unified pseudo-C framework. 2019, *Monthly Notices of the Royal Astronomical Society*, 484, 4127
- Balkenhol, L. & Reichardt, C. L. 2021, The Parameter-Level Performance of Covariance Matrix Conditioning in Cosmic Microwave Background Data Analyses
- Benoit-Lévy, A., Déchelette, T., Benabed, K., et al., Full-sky CMB lensing reconstruction in presence of sky-cuts. 2013, *A&A*, [1301.4145](#)
- Challinor, A. & Chon, G., Error analysis of quadratic power spectrum estimates for CMB polarization: sampling covariance. 2004, *Monthly Notices of the Royal Astronomical Society*, 360, 509, [0410097](#)
- Chon, G., Challinor, A., Prunet, S., Hivon, E., & Szapudi, I., Fast estimation of polarization power spectra using correlation functions. 2004, *MNRAS*, 350, 914, [astro-ph/0303414](#)
- Dodelson, S. & Schneider, M. D., The effect of covariance estimator error on cosmological parameter constraints. 2013, *Physical Review D - Particles, Fields, Gravitation and Cosmology*, 88, 1, [1304.2593](#)
- Dutcher, D., Balkenhol, L., Ade, P. A., et al., Measurements of the e -mode polarization and temperature- e -mode correlation of the CMB from SPT-3G 2018 data. 2021, *Physical Review D*, 104, 22003, [2101.01684](#)
- Efstathiou, G., Myths and truths concerning estimation of power spectra: the case for a hybrid estimator. 2004, *MNRAS*, 349, 603, [astro-ph/0307515](#)
- Friedrich, O., Andrade-Oliveira, F., Camacho, H., et al., Dark energy survey year 3 results: Covariance modelling and its impact on parameter estimation and quality of fit. 2021, *Monthly Notices of the Royal Astronomical Society*, 3165, 3125, [2012.08568](#)
- García-García, C., Alonso, D., & Bellini, E., Disconnected pseudo- Cl covariances for projected large-scale structure data. 2019, *Journal of Cosmology and Astroparticle Physics*, 2019, 043

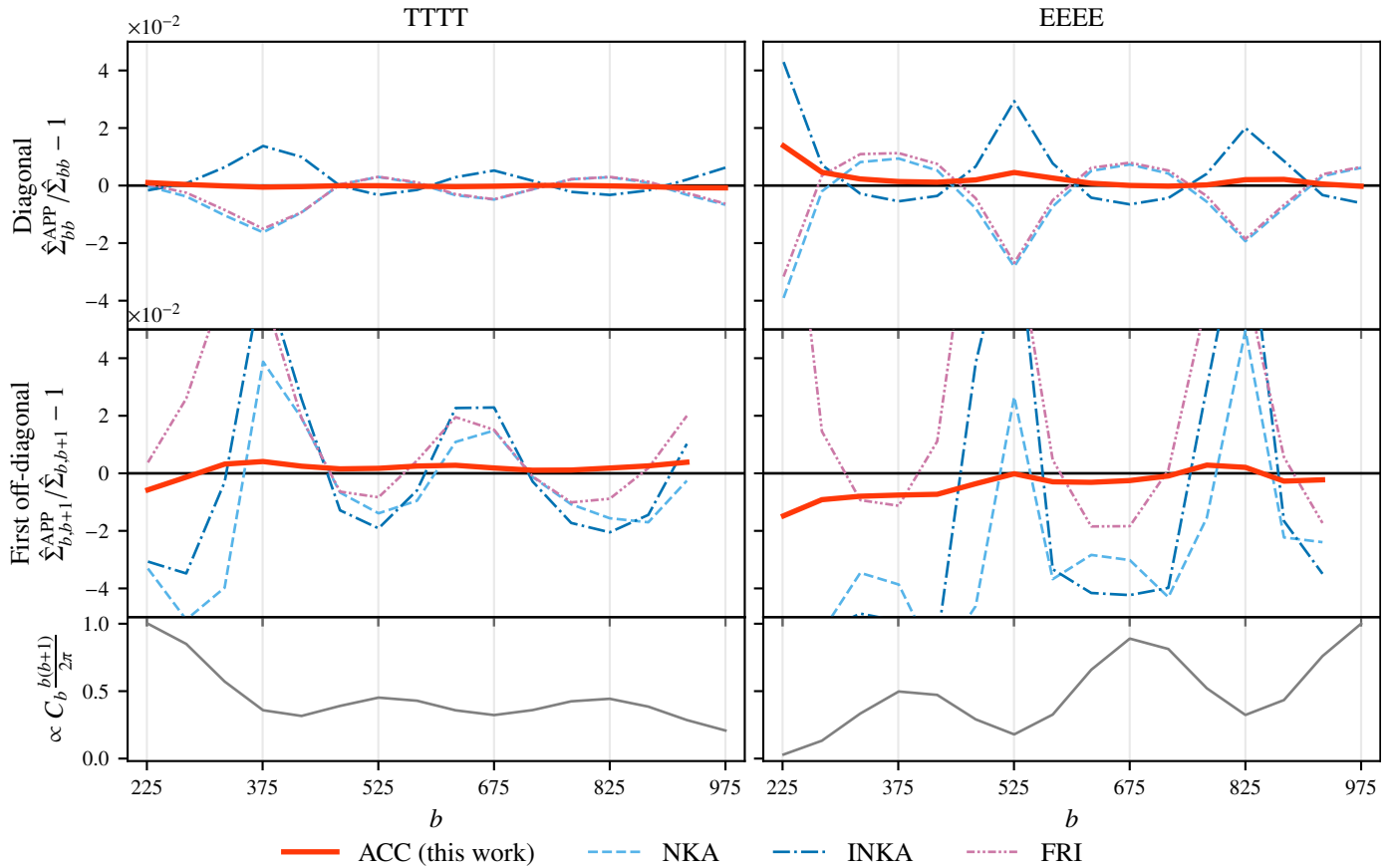


Fig. 14: Relative differences of binned PolSpice covariance matrices calculated using approximations of the pseudo-spectrum covariance with respect to the exact computation: $\hat{\Sigma}_{bb'}^{\text{APP}}/\hat{\Sigma}_{bb'} - 1$, for TTTT (left hand side) and EEEE (right hand side), with binning $\Delta\ell = 50$. On the first row we plot the relative differences for the diagonal, *i.e.* $b = b'$, while on the second row we plot the differences for the first off-diagonal, *i.e.* $b' = b + 1$. Similarly to the case of pseudo-covariances in Fig. 6, we find acceptable accuracy for the NKA (dash light blue), INKA (dash-dot dark blue) and FRI (dash-double-dot purple) approximations, while our ACC approximation (solid red) improves over all of the others. The PolSpice covariance matrices have been calculated using Eqs. (55) and (56). The last row displays the corresponding binned underlying renormalised spectrum TT or EE, to highlight the fact that the differences in the covariances are on the peaks and in the troughs of the spectra, *i.e.* where the spectral variations are maximal.

Gorski, K. M., Hivon, E., Banday, A. J., et al., HEALPix: A Framework for High-Resolution Discretization and Fast Analysis of Data Distributed on the Sphere. 2005, The Astrophysical Journal, 622, 759, [0409513](#)

Gratton, S., Migliaccio, M., Challinor, A., et al., In preparation. 2022

Hazumi, M., Borrill, J., Chinone, Y., et al. 2012, in Proc. SPIE, Vol. 8442, Space Telescopes and Instrumentation 2012: Optical, Infrared, and Millimeter Wave, 844219

Hivon, E., Górski, K. M., Netterfield, C. B., et al., MASTER of the Cosmic Microwave Background Anisotropy Power Spectrum: A Fast Method for Statistical Analysis of Large and Complex Cosmic Microwave Background Data Sets. 2002, ApJ, 567, 2, [arXiv:astro-ph/0105302](#)

Khersonskii, V., Moskalev, A., & Varshalovich, D. 1988, Quantum Theory Of Angular Momentum (World Scientific Publishing Company)

Louis, T., Naess, S., Garrido, X., & Challinor, A., Fast computation of angular power spectra and covariances of high-resolution cosmic microwave background maps using the Toeplitz approximation. 2020, Physical Review D, 102, 123538, [2010.14344](#)

Lueker, M., Reichardt, C. L., Schaffer, K. K., et al., Measurements of secondary cosmic microwave background anisotropies with the South Pole Telescope. 2010, Astrophysical Journal, 719, 1045, [0912.4317](#)

Nicola, A., García-García, C., Alonso, D., et al., Cosmic shear power spectra in practice. 2021, Journal of Cosmology and Astroparticle Physics, 2021, [2010.09717](#)

Planck Collaboration, Aghanim, N., Arnaud, M., et al., Planck 2015 results. XI. CMB power spectra, likelihoods, and robustness of parameters. 2015, A&A, [1507.02704](#)

Planck Collaboration, Aghanim, N., et al., Planck 2018 results. VI. Cosmological parameters. 2020, A&A, 641, A6, [1807.06209](#)

Sellentin, E. & Starck, J. L., Debiasing inference with approximate covariance matrices and other unidentified biases. 2019, Journal of Cosmology and Astroparticle Physics, 2019, [1902.00709](#)

Szapudi, I., Prunet, S., Pogosyan, D., Szalay, A. S., & Bond, J. R., Fast Cosmic Microwave Background Analyses via Correlation Functions. 2001, The Astrophysical Journal, 548, L115

Appendix A: Analysis on the curved sky

This appendix describes the mathematical tools that are used on curved sky for CMB analysis. We make use of the spherical harmonic decomposition of Gaussian fields. We introduce various operators that allow us to express the couplings and the covariance of the power spectra. We make use of some geometrical relations of spherical harmonics to obtain our results. In this appendix, we introduce formulae that can be either used in the temperature or the polarization case.

Appendix A.1: Temperature

We first consider the case of a map of the CMB intensity anisotropies $T(\hat{n})$ observed in direction \hat{n} . The anisotropies are distributed as a Gaussian random field with a corresponding power spectrum C_ℓ^{TT} , observed through a mask $W(\hat{n})$.

Harmonic coefficients and underlying power spectrum

The intensity map can be decomposed with spin-0 spherical harmonics to obtain the harmonic coefficients and their variance, the intensity power spectrum, which fully characterizes the physical properties of the field

$$a_{\ell m}^{\text{T}} = \int d\hat{u} T(\hat{u}) {}_0 Y_{\ell m}^*(\hat{u}), \quad (\text{A.1})$$

$$\langle a_{\ell m}^{\text{T}} a_{\ell' m'}^{\text{T}*} \rangle = C_\ell^{\text{TT}} \delta_{\ell \ell'} \delta_{mm'}. \quad (\text{A.2})$$

Here the brackets $\langle \rangle$ indicate an average over many realizations of the maps.

Weighted mask $W(\hat{n})$

The weighted mask is a real map with weights from 0 to 1 that is used to taper the data on the border of the survey area in order to reduce Fourier ringing when using harmonic decomposition. We define the mask harmonic coefficients and its power spectrum as

$$w_{\ell m} \equiv \int d\hat{u} W(\hat{u}) {}_0 Y_{\ell m}^*(\hat{u}), \quad (\text{A.3})$$

$$\mathcal{W}_\ell \equiv \frac{1}{2\ell + 1} \sum_m w_{\ell m} w_{\ell m}^*. \quad (\text{A.4})$$

Pseudo-power spectrum estimator

In CMB experiments, one way to obtain a biased estimator of the power spectrum is to define the pseudo-harmonic coefficients and the pseudo-power spectrum

$$\tilde{a}_{\ell m}^{\text{T}} \equiv \int d\hat{u} W(\hat{u}) T(\hat{u}) {}_0 Y_{\ell m}^*(\hat{u}), \quad (\text{A.5})$$

$$\tilde{C}_\ell^{\text{TT}} \equiv \frac{1}{2\ell + 1} \sum_{m=-\ell}^{\ell} |\tilde{a}_{\ell m}^{\text{T}}|^2. \quad (\text{A.6})$$

Relation between harmonic coefficients

We relate the masked pseudo-harmonic coefficients to the unmasked one with

$$\tilde{a}_{\ell m}^{\text{T}} = \sum_{\ell' m'} a_{\ell' m'}^{\text{T}} {}_0 I_{\ell m \ell' m'}[W]. \quad (\text{A.7})$$

The $I[W]$ couplings are defined below and can be expressed in terms of sums over Wigner-3j symbols and the $w_{\ell m}$, with

$${}_0 I_{\ell m \ell' m'}[W] \equiv \int d\hat{u} {}_0 Y_{\ell m}(\hat{u}) W(\hat{u}) {}_0 Y_{\ell' m'}^*(\hat{u}), \quad (\text{A.8})$$

$$= \sum_{LM} w_{LM} (-1)^{m'} \left[\frac{(2\ell + 1)(2\ell' + 1)(2L + 1)}{4\pi} \right]^{1/2} \begin{pmatrix} \ell & \ell' & L \\ -s & s & 0 \end{pmatrix} \times \begin{pmatrix} \ell & \ell' & L \\ m & -m' & M \end{pmatrix}. \quad (\text{A.9})$$

Here, we anticipated the extension of this notation to the polarized case which deals with spin-2 fields. The mask-dependent ${}_0 I_{\ell m \ell' m'}[W]$ coupling coefficients relate the underlying harmonic coefficients to the measured pseudo-harmonic coefficients. In the full-sky case, one gets ${}_0 I_{\ell m \ell' m'}[1] = \delta_{\ell \ell'} \delta_{mm'}$ thanks to the closing relations of the spin-weighted spherical harmonics.

Let us introduce some useful relations that are demonstrated in [Hivon et al. \(2002\)](#)

$$\sum_{\ell m} {}_0 I_{\ell_1 m_1 \ell m}[W] {}_0 I_{\ell_2 m_2 \ell m}^*[W] = {}_0 I_{\ell_1 m_1 \ell_2 m_2}[W^2], \quad (\text{A.10})$$

$$\sum_{m_1 m_2} \frac{{}_0 I_{\ell_1 m_1 \ell_2 m_2}[W] {}_0 I_{\ell_1 m_1 \ell_2 m_2}^*[W]}{(2\ell_1 + 1)(2\ell_2 + 1)} = \Xi_{\ell_1 \ell_2}^{ss'}[W]. \quad (\text{A.11})$$

Here we introduced the symmetric operator $\Xi^{ss'}$ acting on a power spectrum \mathcal{A}_ℓ ,

$$\Xi_{\ell \ell'}^{ss'}[\mathcal{A}] \equiv \sum_L \frac{2L + 1}{4\pi} \mathcal{A}_L \begin{pmatrix} \ell & \ell' & L \\ s & -s & 0 \end{pmatrix} \begin{pmatrix} \ell & \ell' & L \\ s' & -s' & 0 \end{pmatrix}. \quad (\text{A.12})$$

We extend this definition to an operator acting on a map $A(\hat{n})$, with

$$\Xi_{\ell \ell'}^{ss'}[A] \equiv \Xi_{\ell \ell'}^{ss'}[\mathcal{A}], \quad (\text{A.13})$$

where we defined the power spectrum \mathcal{A}_ℓ of the map A as in Eqs. (A.3) and (A.4).

MASTER relation between estimated and true spectra

Inserting Eq. (A.5) into Eq. (A.6), using the relations of Eq. (A.11) and the definition of Eq. (A.12)-(A.13), we relate the ensemble average of the pseudo-power spectrum to the underlying power spectrum using the MASTER mode-coupling kernel with

$$\langle \tilde{C}_\ell^{\text{TT}} \rangle = \sum_{\ell'} {}_0 M_{\ell \ell'}[W] C_{\ell'}^{\text{TT}}. \quad (\text{A.14})$$

The MASTER mode-coupling matrix is given by

$${}_0 M_{\ell \ell'}[W] \equiv (2\ell' + 1) \Xi_{\ell \ell'}^{00}[W]. \quad (\text{A.15})$$

Appendix A.2: Polarization

We consider the case of the CMB intensity and polarization anisotropies, represented by maps $T(\hat{n})$, $Q(\hat{n})$, $U(\hat{n})$ in direction \hat{n} of the sky. These are gaussian random fields, fully characterized by their power spectra (C_ℓ^{TT} , C_ℓ^{EE} , C_ℓ^{BB} , C_ℓ^{TE}) observed through a mask $W(\hat{n})$. The definitions and relations of the previous section can be extended to polarization spectra. First we compute

the pseudo-harmonic coefficients on the masked sky with spin weighted spherical harmonics, given in the following inverse relation from Chon et al. (2004)

$$(Q \pm iU)(\hat{n}) = \sum_{\ell m} (\tilde{a}_{\ell m}^E \mp i\tilde{a}_{\ell m}^B) {}_{\mp 2} Y_{\ell m} \quad (\text{A.16})$$

The pseudo-power spectrum $\tilde{C}_{\ell}^{\text{XY}}$ is obtained by summing over the measured pseudo-harmonic coefficients $\tilde{a}_{\ell m}^X$, $X, Y \in [T, E, B]$ with the same multipole ℓ , with

$$\tilde{C}_{\ell}^{\text{XY}} = \frac{1}{2\ell + 1} \sum_{m=-\ell}^{\ell} \tilde{a}_{\ell m}^X \tilde{a}_{\ell m}^{Y*} \quad (\text{A.17})$$

More details can be found in Challinor & Chon (2004). Following the same approach as in the previous section, one can write the MASTER relation in polarization

$$\langle \tilde{C}_{\ell}^{\text{EE}} + \tilde{C}_{\ell}^{\text{BB}} \rangle = \sum_{\ell'} {}_{+2} M_{\ell \ell'} (C_{\ell'}^{\text{EE}} + C_{\ell'}^{\text{BB}}), \quad (\text{A.18})$$

$${}_{+2} M_{\ell \ell'} = (2\ell' + 1) \Xi_{\ell \ell'}^{22} [W], \quad (\text{A.19})$$

$$\langle \tilde{C}_{\ell}^{\text{EE}} - \tilde{C}_{\ell}^{\text{BB}} \rangle = \sum_{\ell'} {}_{-2} M_{\ell \ell'} (C_{\ell'}^{\text{EE}} - C_{\ell'}^{\text{BB}}), \quad (\text{A.20})$$

$${}_{-2} M_{\ell \ell'} = (2\ell' + 1) \Xi_{\ell \ell'}^{2-2} [W], \quad (\text{A.21})$$

$$\langle \tilde{C}_{\ell}^{\text{TE}} \rangle = \sum_{\ell'} {}_{\times} M_{\ell \ell'} C_{\ell'}^{\text{TE}}, \quad (\text{A.22})$$

$${}_{\times} M_{\ell \ell'} = (2\ell' + 1) \Xi_{\ell \ell'}^{20} [W]. \quad (\text{A.23})$$

Appendix A.3: Renormalised kernels

We define the renormalised MASTER kernels, which will be used in the INKA approximation. They are written as

$${}_{\mathbf{k}} \tilde{M}_{\ell \ell'} \equiv \frac{1}{\sum_{\ell' \mathbf{k}} M_{\ell \ell'}} {}_{\mathbf{k}} M_{\ell \ell'}, \quad \forall \mathbf{k} \in [0, -2, +2, \times]. \quad (\text{A.24})$$

Summing over ℓ' yields

$$\sum_{\ell'} {}_{\mathbf{k}} \tilde{M}_{\ell \ell'} = 1, \quad (\text{A.25})$$

which ensures that the approximated covariance coupling kernel defined in Eq. (30) is properly normalized.

Appendix B: Covariance of the pseudo-power spectrum

In this appendix, we outline how the formula of the covariance matrix of the pseudo-power spectrum is obtained, in the temperature case. Our goal is to introduce Eq. (B.9). The covariance matrix of the pseudo-power spectrum writes

$$\begin{aligned} \tilde{\Sigma}_{\ell \ell'} &= \langle \tilde{C}_{\ell} \tilde{C}_{\ell'} \rangle - \langle \tilde{C}_{\ell} \rangle \langle \tilde{C}_{\ell'} \rangle, \\ &= \sum_{mm'} \frac{\langle |\tilde{a}_{\ell m}|^2 |\tilde{a}_{\ell' m'}|^2 \rangle - \langle |\tilde{a}_{\ell m}|^2 \rangle \langle |\tilde{a}_{\ell' m'}|^2 \rangle}{(2\ell + 1)(2\ell' + 1)}. \end{aligned} \quad (\text{B.1})$$

As the intensity map $T(\hat{n})$ is real and the spherical harmonics follow

$${}_0 Y_{\ell m}^* = (-1)^m {}_0 Y_{\ell(-m)}, \quad (\text{B.2})$$

the spherical harmonic coefficients of $T(\hat{n})$ follow

$$a_{\ell m}^* = (-1)^m a_{\ell(-m)}. \quad (\text{B.3})$$

Then, when computing the four-point function, and thanks to Wick's theorem,

$$\begin{aligned} &\sum_{mm'} \langle |\tilde{a}_{\ell m}|^2 |\tilde{a}_{\ell' m'}|^2 \rangle - \langle |\tilde{a}_{\ell m}|^2 \rangle \langle |\tilde{a}_{\ell' m'}|^2 \rangle \\ &= \sum_{mm'} \langle \tilde{a}_{\ell m} \tilde{a}_{\ell' m'} \rangle \langle \tilde{a}_{\ell m}^* \tilde{a}_{\ell' m'}^* \rangle + \langle \tilde{a}_{\ell m} \tilde{a}_{\ell' m'}^* \rangle \langle \tilde{a}_{\ell m}^* \tilde{a}_{\ell' m'} \rangle. \end{aligned} \quad (\text{B.4})$$

Looking at the first term of this sum, and using the change of variable $m'' = -m'$, it is straightforward to show that

$$\begin{aligned} &\sum_{mm'} \langle \tilde{a}_{\ell m} \tilde{a}_{\ell' m'} \rangle \langle \tilde{a}_{\ell m}^* \tilde{a}_{\ell' m'}^* \rangle \\ &= \sum_{mm'} (-1)^{(2m')} \langle \tilde{a}_{\ell m} \tilde{a}_{\ell'(-m')}^* \rangle \langle \tilde{a}_{\ell m}^* \tilde{a}_{\ell'(-m')} \rangle, \\ &= \sum_{mm''} \langle \tilde{a}_{\ell m} \tilde{a}_{\ell' m''}^* \rangle \langle \tilde{a}_{\ell m}^* \tilde{a}_{\ell' m''} \rangle. \end{aligned} \quad (\text{B.5})$$

Finally, one has

$$\begin{aligned} &\sum_{mm'} \langle |\tilde{a}_{\ell m}|^2 |\tilde{a}_{\ell' m'}|^2 \rangle - \langle |\tilde{a}_{\ell m}|^2 \rangle \langle |\tilde{a}_{\ell' m'}|^2 \rangle, \\ &= 2 \sum_{mm'} \langle \tilde{a}_{\ell m} \tilde{a}_{\ell' m'}^* \rangle \langle \tilde{a}_{\ell m}^* \tilde{a}_{\ell' m'} \rangle \\ &= 2 \sum_{mm'} |\langle \tilde{a}_{\ell m} \tilde{a}_{\ell' m'}^* \rangle|^2. \end{aligned} \quad (\text{B.6})$$

Then, one has, for the covariance matrix,

$$\tilde{\Sigma}_{\ell \ell'} = \frac{2}{(2\ell + 1)(2\ell' + 1)} \sum_{mm'} |\langle \tilde{a}_{\ell m} \tilde{a}_{\ell' m'}^* \rangle|^2. \quad (\text{B.7})$$

Using the decomposition of pseudo-harmonic coefficients, yields

$$\begin{aligned} \langle \tilde{a}_{\ell m} \tilde{a}_{\ell' m'}^* \rangle &= \sum_{\ell_1 m_1 \ell_2 m_2} \langle a_{\ell_1 m_1} a_{\ell_2 m_2}^* \rangle I_{\ell m \ell_1 m_1} [W] I_{\ell' m' \ell_2 m_2}^* [W], \\ &= \sum_{\ell_1 m_1} C_{\ell_1} I_{\ell m \ell_1 m_1} [W] I_{\ell' m' \ell_1 m_1}^* [W]. \end{aligned} \quad (\text{B.8})$$

Inserting Eq. (B.8) into Eq. (B.7) gives

$$\begin{aligned} \tilde{\Sigma}_{\ell \ell'} &= \frac{2}{(2\ell + 1)(2\ell' + 1)} \sum_{mm'} \sum_{\ell_1 m_1} \sum_{\ell_2 m_2} C_{\ell_1} C_{\ell_2} \\ &\quad I_{\ell m \ell_1 m_1} [W] I_{\ell' m' \ell_1 m_1}^* [W] I_{\ell m \ell_2 m_2}^* [W] I_{\ell' m' \ell_2 m_2} [W]. \end{aligned} \quad (\text{B.9})$$

Appendix C: Expansion in Legendre series

In this section, we introduce the Legendre transforms of the harmonic quantities used in this work. Each relation in harmonic space has a corresponding expression in real space. The PolSpice software relies on the relations in real space.

Appendix C.1: From spin-0 spectra to two point correlation functions

Given a spectrum \mathcal{A}_{ℓ} , one can associate with it a real two-point correlation function a

$$a(\theta) = \sum_{\ell} \frac{2\ell + 1}{4\pi} \mathcal{A}_{\ell} P_{\ell}(\cos \theta) \quad \forall \theta \in [0, \pi]. \quad (\text{C.1})$$

The inverse relation is

$$\mathcal{A}_\ell = 2\pi \int_0^\pi d\theta \sin \theta a(\theta) P_\ell(\cos \theta) \quad \forall \ell \geq 0. \quad (\text{C.2})$$

The two-point function gives the correlations between two directions of the sky, for instance in the CMB anisotropies full sky case, we can write

$$\langle T(\hat{n}_1)T(\hat{n}_2) \rangle = \sum_\ell \frac{2\ell + 1}{4\pi} C_\ell^{\text{TT}} P_\ell(\hat{n}_1 \cdot \hat{n}_2). \quad (\text{C.3})$$

Appendix C.2: From convolution to multiplication

A convolution with a square matrix A in harmonic space, such as in Eq. (A.14) is equivalent to a multiplication in real space with the correlation function $a(\theta)$ given by

$$a(\theta) \frac{2\ell' + 1}{4\pi} P_{\ell'}(\cos \theta) = \sum_\ell \frac{2\ell + 1}{4\pi} A_{\ell\ell'} \quad \forall \theta \in [0, \pi]. \quad (\text{C.4})$$

The inverse relation is

$$A_{\ell\ell'} \equiv \frac{2\ell' + 1}{2} \int_0^\pi a(\theta) P_\ell(\cos \theta) P_{\ell'}(\cos \theta) \sin(\theta) d\theta. \quad (\text{C.5})$$

The last relation is equivalent to

$$A_{\ell\ell'} = (2\ell' + 1) \Xi_{\ell\ell'}^{00} [\mathcal{A}], \quad (\text{C.6})$$

with \mathcal{A} the power spectrum associated with the two-point function a through a Legendre transform. We can thus extend the definition of the operator Ξ to an operator acting on a correlation function a , with

$$\Xi_{\ell\ell'}^{ss'} [a] \equiv \Xi_{\ell\ell'}^{ss'} [\mathcal{A}]. \quad (\text{C.7})$$

Here we have already extended the definition to be used in the spin-2 case, which we discuss in the next subsection.

Appendix C.3: Spin-2

Similar rules to the ones introduced above can be written for spin-2 quantities, by replacing the Legendre polynomials by more general reduced Wigner d -matrix $d_{2\pm 2}^\ell$. Details can be found in Challinor & Chon (2004). The spin-2 relations are, for the \mathcal{A}_ℓ^\pm power spectra associated with a spin-2 field

$$a_\pm(\theta) = \sum_\ell \frac{2\ell + 1}{4\pi} \beta_\ell d_{2\pm 2}^\ell(\cos \theta), \quad (\text{C.8})$$

$$\mathcal{A}_\ell^\pm = 2\pi \int_0^\pi d\theta \sin \theta a_\pm(\theta) d_{2\pm 2}^\ell(\cos \theta). \quad (\text{C.9})$$

We can associate a correlation function with its spin-2 convolution matrix,

$$\begin{aligned} \pm A_{\ell\ell'} &= \frac{2\ell' + 1}{2} \int_0^\pi a(\theta) d_{2\pm 2}^\ell(\cos \theta) d_{2\pm 2}^{\ell'}(\cos \theta) \sin(\theta) d\theta, \\ &= (2\ell' + 1) \Xi_{\ell\ell'}^{2\pm 2} [a]. \end{aligned} \quad (\text{C.10})$$

We can also compute the matrix associate with the spin-0 cross spin-2 case

$$\times A_{\ell\ell'} = (2\ell' + 1) \Xi_{\ell\ell'}^{20} [a]. \quad (\text{C.11})$$

Appendix C.4: Applying this formalism to the MASTER matrix

In our case, we can write, for $s \in [0, 2]$,

$${}_\pm M_{\ell\ell'} = (2\ell' + 1) \Xi_{\ell\ell'}^{s\pm s} [w] \quad (\text{C.12})$$

with $w(\theta)$ the correlation function of the mask.

Let us apply the previous formalism and particularly the Eq. (C.12) to the MASTER relation. We use Legendre series expansion of the true power spectrum C_ℓ and the pseudo-power spectrum estimator \tilde{C}_ℓ to define the correlation functions ξ and $\tilde{\xi}$ respectively. It gives

$$\tilde{\xi}(\theta) \equiv \sum_\ell \frac{2\ell + 1}{4\pi} P_\ell(\cos \theta) \tilde{C}_\ell, \quad (\text{C.13})$$

$$\xi(\theta) \equiv \sum_\ell \frac{2\ell + 1}{4\pi} P_\ell(\cos \theta) C_\ell. \quad (\text{C.14})$$

Starting from the right hand side of Eq. (34) and going to real space using a Legendre transform at an angle $\theta \in [0, \pi]$, we have

$$\begin{aligned} \sum_{\ell\ell'} \frac{2\ell + 1}{4\pi} P_\ell(\cos \theta) {}_0 M_{\ell\ell'} C_{\ell'} \\ = \sum_{\ell'} w(\theta) \frac{2\ell' + 1}{4\pi} P_{\ell'}(\cos \theta) C_{\ell'}, \\ = w(\theta) \tilde{\xi}(\theta), \end{aligned}$$

which implies $\langle \tilde{\xi}(\theta) \rangle = w(\theta) \tilde{\xi}(\theta)$.

with $w(\theta)$ the correlation function of the mask.

Appendix C.5: PolSpice in polarization

This section aims at describing the regularization technique used for polarization by PolSpice. One of the main advantages of PolSpice is that it allows the possibility of eliminating EE to BB (and BB to EE) mixing, using non-local relations between Wigner d -matrices, see Sec. 5 of Chon et al. (2004). The obtained estimator \hat{C}_ℓ^{EE} (respectively \hat{C}_ℓ^{BB}) depends only on the average of C_ℓ^{EE} (respectively C_ℓ^{BB}) and the scalar apodizing function f .

Using the Legendre transforms of spin-2 quantities (Eq. (C.9)), let us associate the correlation functions ξ_\pm with the spectra $C_\ell^{\text{EE}} \pm C_\ell^{\text{BB}}$ and $\tilde{\xi}_\pm$ to $\tilde{C}_\ell^{\text{EE}} \pm \tilde{C}_\ell^{\text{BB}}$. PolSpice builds two correlation functions $\hat{\xi}_{\text{dec}}$ and $\hat{\xi}_-$ to produce an estimator of the true underlying polarized power spectrum. The latter is defined similarly to $\hat{\xi}$ in Eq. (39),

$$\hat{\xi}_-(\theta) = g(\theta) \tilde{\xi}_-(\theta). \quad (\text{C.16})$$

The first is built on integral relations. PolSpice eliminates the mixing inherent in $\tilde{\xi}_+$ with the following relation in real space,

$$\hat{\xi}_{\text{dec}}(\theta) = g(\theta) \int_{-1}^1 d\cos \theta' \tilde{\xi}_+(\theta') \sum_\ell d_{2-2}^\ell(\theta) d_{22}^\ell(\theta'). \quad (\text{C.17})$$

This correlation function is noted with the subscript dec to emphasize that it is the crucial step allowing the decoupling of the polarized estimator. When averaging out Eq. (C.16) and Eq. (C.17) on multiple realizations,

$$\langle \hat{\xi}_{\text{dec}}(\theta) \rangle = f(\theta) \int_{-1}^1 d\cos \theta' \xi_+(\theta') \sum_\ell d_{2-2}^\ell(\theta) d_{22}^\ell(\theta'), \quad (\text{C.18})$$

$$\langle \hat{\xi}_-(\theta) \rangle = f(\theta) \xi_-(\theta). \quad (\text{C.19})$$

In harmonic space, transforming Eq. (C.18) and Eq. (C.19) using d_{2-2}^ℓ , it gives, with ${}_{-2}K_{\ell\ell'} = (2\ell' + 1)\Xi_{\ell\ell'}^{2-2}[f^{\text{apo}}]$,

$$\hat{C}_\ell^{\text{EE}} + \hat{C}_\ell^{\text{BB}} \equiv 2\pi \int_0^\pi d\cos\theta \hat{\xi}_{\text{dec}}(\theta) d_{2-2}^\ell(\theta), \quad (\text{C.20})$$

$$\hat{C}_\ell^{\text{EE}} - \hat{C}_\ell^{\text{BB}} \equiv 2\pi \int_0^\pi d\cos\theta \hat{\xi}_-(\theta) d_{2-2}^\ell(\theta), \quad (\text{C.21})$$

which implies

$$\langle \hat{C}_\ell^{\text{EE}} \pm \hat{C}_\ell^{\text{BB}} \rangle = \sum_{\ell'} {}_{-2}K_{\ell\ell'}(C_{\ell'}^{\text{EE}} \pm C_{\ell'}^{\text{BB}}). \quad (\text{C.22})$$

Summing or subtracting the last equation for + or - allows one to build unmixed estimators of the polarization power spectra. If one had chosen not to decouple the correlation functions and had built $\hat{C}_\ell^{\text{EE}} + \hat{C}_\ell^{\text{BB}}$ as the Legendre transform of $\hat{\xi}_+ = g\tilde{\xi}_+$, the output PolSpice spectra would follow

$$\langle \hat{C}_\ell^{\text{EE}} \pm \hat{C}_\ell^{\text{BB}} \rangle = \sum_{\ell'} {}_{\pm 2}K_{\ell\ell'}(C_{\ell'}^{\text{EE}} \pm C_{\ell'}^{\text{BB}}), \quad (\text{C.23})$$

which would leave some mixing in the polarization spectra, given that ${}_{+2}K \neq {}_{-2}K$.

Appendix D: Multi-mask analysis

In this section, we will generalize our analysis to multiple masks. This situation occurs when performing cross-power spectrum analysis with maps with different masks. We shall restrict ourselves to the study of the intensity case. Writing the expression of the covariance explicitly as in García-García et al. (2019), one has the following expression

$$\begin{aligned} \text{cov}(\tilde{C}_\ell^{i,j}, \tilde{C}_{\ell'}^{p,q}) &= \frac{1}{(2\ell+1)(2\ell'+1)} \sum_{mm'} [\langle \tilde{a}_{\ell m}^i \tilde{a}_{\ell' m'}^p \rangle^* \langle \tilde{a}_{\ell m}^{j*} \tilde{a}_{\ell' m'}^q \rangle + (p \leftrightarrow q)], \\ &= \frac{1}{(2\ell+1)(2\ell'+1)} \sum_{\ell_1 \ell_2} \sum_{m_1 m_2 m m'} [C_{\ell_1}^{i,p} I_{k_1 k_1} [W^i] I_{k_1 k'} [W^p] \\ &\quad C_{\ell_2}^{j,q} I_{k_2 k} [W^j] I_{k' k_2} [W^q] + (p \leftrightarrow q)], \\ &= \Xi_{\ell\ell'}^{00} [W^i, W^p, W^j, W^q] \sum_{\ell_1 \ell_2} [C_{\ell_1}^{i,p} \bar{\Theta}_{\ell\ell'}^{\ell_1 \ell_2} [W^i, W^p, W^j, W^q] C_{\ell_2}^{j,q} + \\ &\quad (p \leftrightarrow q)]. \end{aligned}$$

We noted $k_i = (\ell_i, m_i)$. We also extended the definition of the kernels to the case multiple masks as

$$\Xi_{\ell\ell'}^{00} [W^i, W^p] (W^j, W^q) \equiv \Xi_{\ell\ell'}^{00} [\mathcal{V}^{(ip) \times (jq)}], \quad (\text{D.1})$$

$$\text{where } \mathcal{V}_\ell^{(ip) \times (jq)} \equiv \frac{1}{2\ell+1} \sum_m [W^i W^p]_{\ell m} [W^j W^q]_{\ell m}^*, \quad (\text{D.2})$$

$$\begin{aligned} \Theta_{\ell\ell'}^{\ell_1 \ell_2} [W^i, W^p, W^j, W^q] &= \sum_{mm' m_1 m_2} I_{\ell m \ell_1 m_1} [W^i] \\ &\quad I_{\ell_1 m_1 \ell' m'} [W^p] I_{\ell' m' \ell_2 m_2} [W^j] I_{\ell_2 m_2 \ell m} [W^q]. \end{aligned} \quad (\text{D.3})$$

As long as the masks considered have similar properties, for instance that none of them include point sources, the computations developed in this work will hold. Indeed, in Eq. (E.2), the assumptions hold as long as the mask harmonic coefficients fall quickly enough, which is the case even if the survey area varies a little from one map to another.

Appendix E: Details on the ACC approximation

Appendix E.1: Mathematical validation

Let us explore why the mathematical justification of the ACC approximation. From Fig. 9, the $\bar{\Theta}_{\ell\ell'}^{\ell_1 \ell_2}$ kernel seems to only depend on $\Delta \equiv \ell' - \ell$, $\Delta_1 \equiv \ell_1 - \ell$ and $\Delta_2 \equiv \ell_2 - \ell$. We recall that the normalization of the reduced coupling kernel (Eq. (22)) already approximately only depends on Δ , since $\Xi_{\ell\ell'}^{00}$ is close to a Toeplitz matrix (Louis et al. 2020). The kernel itself is given by a summation of products of four coupling coefficients ${}_0I_{\ell m_1 m_1}$. Those are expressed as the sum of the mask window function with a product of two Wigner-3j symbols, as shown in Eq. (A.9). One can remark that since the mask power spectrum falls relatively fast (Fig. 1), mostly the terms with low L in the sum in Eq. (A.9) will contribute. However, we are interested in the cases where all of the other multipoles ℓ, ℓ', ℓ_1 and ℓ_2 are significantly larger than the width of the mask spectrum. For this reason, all of the Wigner-3j symbols in Eq. (A.9) can be replaced by their asymptotic behavior, where in the limit $\ell_i, \ell_j \gg L_i$, we have

$$\begin{pmatrix} \ell_i & \ell_j & L_i \\ m_i & m_j & M_i \end{pmatrix} \approx \frac{(-1)^{\ell_j+m_j}}{\sqrt{2\ell_j+1}} d_{M_i, (\ell_j-\ell_i)}^{L_i}(\theta), \quad (\text{E.1})$$

(Khersonskii et al. 1988). Here, $\theta = \arccos(-m_j/(\ell_j(\ell_j+1))^{1/2})$ and $d_{k,m}^j$ are reduced Wigner rotation matrices.

Introducing this approximation in Eq. (A.9), Eq. (21) now reads

$$\begin{aligned} \Theta_{\ell_3 \ell_4}^{\ell_1 \ell_2} &\approx \frac{1}{(4\pi)^2} \sum_{L_i M_i} \Pi_i w_{L_i M_i} \sqrt{2L_i + 1} d_{0, (\ell_{i+1} - \ell_i)}^{L_i}(\pi/2) \\ &\quad \left[\sum_{m_i} d_{M_i, (\ell_{i+1} - \ell_i)}^{L_i} \left(\arccos \frac{-m_{i+1}}{(\ell_{i+1}(\ell_{i+1}+1))^{1/2}} \right) \right]. \end{aligned} \quad (\text{E.2})$$

Here we have defined $\ell_5 \equiv \ell_1$ for notational purposes. We note that, when ℓ_i are large enough, which is the case since $\ell_i, \ell_j \gg L_i$, $\arccos \frac{-m_{i+1}}{(\ell_{i+1}(\ell_{i+1}+1))^{1/2}}$ explore the $[0, \pi]$ range, and the expression in brackets in the last equation can be seen as a Riemann sum over $\theta \in [0, \pi]$. This expression can be approximated by the integral $\int d_{M_i, (\ell_{i+1} - \ell_i)}^{L_i}(\theta) d\theta$ which only depends on L_i, M_i and $\ell_{i+1} - \ell_i$. Since the L_i, M_i are summed over in Eq. (E.2), we directly see that as soon as ℓ, ℓ', ℓ_1 and ℓ_2 are significantly larger than the width of the mask spectrum, the coupling kernel behaves as a function of their difference, and we expect that this approximation improves in accuracy with ℓ .

Appendix E.2: EE expression

For now, if we ignore BB to EE leakage, we can write

$$\tilde{\Xi}_{\ell\ell'}^{\text{EEE}} \approx 2\Xi_{\ell\ell'}^{22} [W^2] [C^{\text{EE}} \cdot \bar{\Theta}_{\ell\ell'}^{++++} [W] \cdot C^{\text{EE}}] \quad (\text{E.3})$$

where we defined the polarized covariance coupling

$$\Theta_{\ell\ell'}^{\ell_1 \ell_2;++++} = \sum_{mm' m_1 m_2} I_{\ell m \ell_1 m_1} + I_{\ell_1 m_1 \ell' m'} + I_{\ell' m' \ell_2 m_2} + I_{\ell_2 m_2 \ell m}. \quad (\text{E.4})$$

Thanks to relations in Challinor & Chon (2004), this kernel Θ^{++++} can be approximately normalized to

$$\sum_{\ell_1 \ell_2} \Theta_{\ell\ell'}^{\ell_1 \ell_2;++++} [W] \approx \Xi_{\ell\ell'}^{22} [W^2], \quad (\text{E.5})$$

hence the relation (E.3).